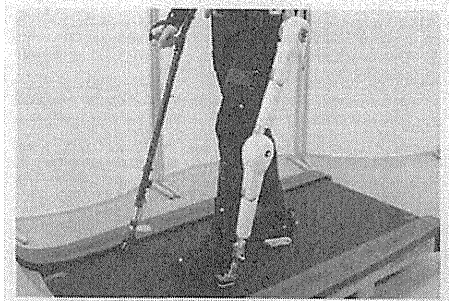

Fig. 7. System setup for the evaluation experiment.

we fixed three FSR sensors on the bottom of the cane to detect these events, and we simply change the parameters of the controllers according to the current gait phase.

IV. Performance Evaluation

To evaluate the proposed method, we conducted an experiment for walking support with single leg version of robot suit HAL. Robot suit HAL is an exoskeleton type assistive robot that can augment human power and support people with mobility impairment [7], and the single leg version of HAL [6] was originally developed for support of hemiplegia patients.

We have developed a real-time control system for the robot based on the motion capture system. For practical application IMU sensors are used to detect the specific body and cane movement. However, we used the motion capture system MAC3D (Motion Analysis Inc.) for sensing whole body movement in the testing phase. One subject was asked to walk on the treadmill with the HAL suit on his left leg and the cane in his right arm, while reflexive markers were attached on several anatomical landmarks of his body and the cane. (Fig.7).

Using the motion capture system we captured the motion of the subject and the cane at 120 fps. The ground contact was obtained from the FSR sensors installed at the tip of the cane via wireless communication. We developed a control system which computes the reference trajectory for the left leg using the principal components matrix we acquired from the analysis with the motion data of the right leg and the cane at each time frame. We used simple PD controllers for the robot's hip and knee joints to operate the robot suit HAL. The gains of the controllers were tuned in advance for the subject for the stance and swing phases. The control commands are transmitted to HAL through wireless network.

Fig.8 plots from top to bottom the angle trajectories of the right hip and knee angles, the cane's angle trajectory, FSR sensors reading, and then the corresponding hip and knee joints of the robot. Both the hip and knee trajectories were close to natural with good cycle to cycle consistency. There was a small tendency to smaller robot hip flexion and knee

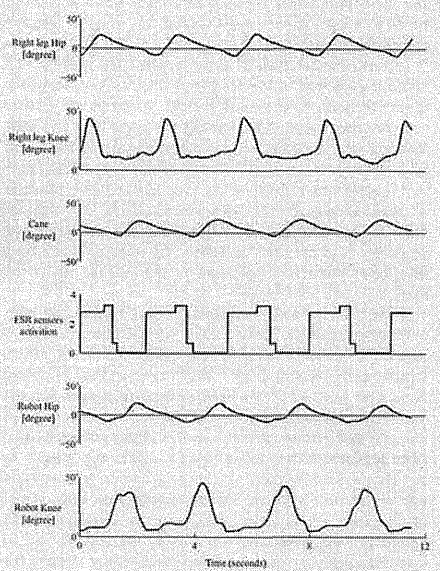

Fig. 8. Signals of the right leg hip and knee angles, cane angle, FSR sensors reading, and the corresponding hip and knee angles operated by robot suit HAL during the experiment.

extension relative to the healthy leg. Overall, we were able to control the robot in real-time according to the subject's intent, based on the movement of the right leg, cane, and cane's ground contact information.

V. Discussion and Conclusions

In this study, we proposed a novel method to control an exoskeleton robot by using the coupling of upper and lower limbs in gait by exploiting the cane. The system emphasis on normal motion in the lower limbs and on arms swing as well. We believe that finding an intuitive and feasible interface between human and robot is essential for practical use of assistive technology, as well as insuring the safety and stability of the human end. In the same time, upper and lower limbs coordination should be considered for an overall healthy gait pattern.

From the experimental results, we found that similar synergies represented by Principal Components were responsible for the motion of lower limbs, upper and lower limbs, and the cane and lower limbs. Therefore, we proposed that the cane is used in such a manner that it falls into the interjoint coordination of human gait, and can capture the arm's motion. Also the angle between the first PCs of the cane

and the contra-lateral leg trajectories was small in average (< 10°) which also indicates a similar way of using the cane among the subjects.

In experimental evaluation we verified the system with single leg version of the HAL suit, and we confirmed the applicability of the proposed method. Although the motion capture system is used for sensing the lower limb and cane movement in this study, wearable sensors such as IMUs can be used for practical application. Additionally, we also plan to investigate the usability of the cane in intention estimation of other locomotion tasks. Such as detecting the start and end of walk from body posture and patterns of acceleration and deceleration of the cane, and detecting standing and sitting from body posture and pressure patterns on the tip of the cane.

So far we have only examined the proposed system with one healthy subject. Testing with several healthy subjects should be carried out with qualitative criteria to affirm specific enhancement in the control system from using the cane. Also, a stroke patient depending on the cane to support his body weight and balance might not be able to coordinate the cane well with his gait. However, walking with assistance from the exoskeleton robot should enable the patient to use the cane more freely, and depend less on it to support his weight and balance. Future investigation with actual stroke patients is to address this issue by investigating the intra/inter limb adaptation when using the system, and to verify the usability and benefit of the proposed method for utilizing the upper and lower limb synergies in rehabilitation of hemiplegic patients after stroke.

ACKNOWLEDGMENT

This study was supported by: the Funding Program for World-Leading Innovative R&D on Science and Technology (FIRST Program).

References

[1] T. Hayashi, H. Kawamoto, and Y. Sankai, "Control method of robot suit HAL working as operator's muscle using biological and dynamical information," in *Intelligent Robots and Systems, 2005. (IROS 2005). 2005 IEEE/RSJ International Conference on*, aug. 2005, pp. 3063 – 3068.

[2] K. Suzuki, Y. Kawamura, T. Hayashi, T. Sakurai, Y. Hasegawa, and Y. Sankai, "Intention-based walking support for paraplegia patient," in *Systems, Man and Cybernetics, 2005 IEEE International Conference on*, vol. 3, oct. 2005, pp. 2707 – 2713 Vol. 3.

[3] H. Vallery, E. van Asseldonk, M. Buss, and H. van der Kooij, "Reference trajectory generation for rehabilitation robots: Complementary limb motion estimation," *Neural Systems and Rehabilitation Engineering, IEEE Transactions on*, vol. 17, no. 1, pp. 23 –30, feb. 2009.

[4] K. A. Strausser and H. Kazerooni, "The development and testing of a human machine interface for a mobile medical exoskeleton," in *Intelligent Robots and Systems (IROS), 2011 IEEE/RSJ International Conference on*, sept. 2011, pp. 4911 –4916.

[5] A. Duschau-Wicke, J. von Zitzewitz, A. Caprez, L. Lunenburger, and R. Riener, "Path control: A method for patient-cooperative robot-aided gait rehabilitation," *Neural Systems and Rehabilitation Engineering, IEEE Transactions on*, vol. 18, no. 1, pp. 38–48, feb. 2010.

[6] H. Kawamoto, T. Hayashi, T. Sakurai, K. Eguchi, and Y. Sankai, "Development of single leg version of HAL for hemiplegia," in *Engineering in Medicine and Biology Society, 2009. EMBC 2009. Annual International Conference of the IEEE*, sept. 2009, pp. 5038 –5043.

[7] Y. Sankai, "HAL: Hybrid assistive limb based on cybernics," in *Robotics Research*, ser. Springer Tracts in Advanced Robotics, M. Kaneko and Y. Nakamura, Eds. Springer Berlin / Heidelberg, 2011, vol. 66, pp. 25–34.

[8] H. Vallery and M. Buss, "Complementary limb motion estimation based on interjoint coordination using principal components analysis," in *Computer Aided Control System Design, 2006 IEEE International Conference on Control Applications, 2006 IEEE International Symposium on Intelligent Control, 2006 IEEE*, oct. 2006, pp. 933 –938.

[9] M. P. Ford, R. C. Wagenaar, and K. M. Newell, "Arm constraint and walking in healthy adults," *Gait & Posture*, vol. 26, no. 1, pp. 135 – 141, 2007.

[10] V. Dietz, K. Fouad, and C. M. Bastiaanse, "Neuronal coordination of arm and leg movements during human locomotion," *The European journal of neuroscience*, vol. 14, pp. 1906–1914, dec. 2001.

[11] T. Wannier, C. Bastiaanse, G. Colombo, and Dietz, "Arm to leg coordination in humans during walking, creeping and swimming activities," *Experimental brain research*, vol. 141, no. 3, pp. 375–379, 2001.

[12] J. E. Balter and E. P. Zehr, "Neural coupling between the arms and legs during rhythmic locomotor-like cycling movement," *Journal of neurophysiology*, vol. 97, no. 2, pp. 1809 – 1818, 2007.

[13] V. Dietz, "Quadrupedal coordination of bipedal gait: implications for movement disorders," *Journal of Neurology*, vol. 258, pp. 1406–1412, 2011.

[14] D. P. Ferris, H. J. Huang, and P.-C. Kao, "Moving the arms to activate the legs," *Exercise and Sport Sciences Reviews*, vol. 34, pp. 113–120, 2006.

[15] J. L. Stephenson, A. Lamontagne, and S. J. D. Serres, "The coordination of upper and lower limb movements during gait in healthy and stroke individuals," *Gait & Posture*, vol. 29, no. 1, pp. 11 – 16, 2009.

[16] A. L. Behrman and S. J. Harkema, "Locomotor training after human spinal cord injury: A series of case studies," *Physical Therapy*, vol. 80, no. 7, pp. 688–700, July 2000.

[17] T.-S. Kuan, J.-Y. Tsou, and F.-C. Su, "Hemiplegic gait of stroke patients: The effect of using a cane," *Archives of Physical Medicine and Rehabilitation*, vol. 80, no. 7, pp. 777 – 784, 1999.

[18] H. Buteni and B. E. Maki, "Assistive devices for balance and mobility: Benefits, demands, and adverse consequences," *Archives of Physical Medicine and Rehabilitation*, vol. 86, no. 1, pp. 134 – 145, 2005.

[19] I. Jolliffe, *Principal component analysis*, ser. Springer series in statistics. Springer-Verlag, 2002.

[20] N. St-Onge and A. Feldman, "Interjoint coordination in lower limbs during different movements in humans," *Experimental Brain Research*, vol. 148, pp. 139–149, 2003.

[21] E. Batschelet, *Circular statistics in biology*, ser. Mathematics in biology. Academic Press, 1981.

[22] J. Perry, *Gait analysis: normal and pathological function*. SLACK, 1992.

2012 IEEE/SICE International Symposium on System Integration (SII)
Kyushu University, Fukuoka, Japan
December 16-18, 2012

Development of 3D Visual Feedback System for Cybernic Master System

Kousuke Hiramatsu and Yoshiyuki Sankai

Abstract— This paper developed 3D Visual Feedback System for Cybernic Master System. This Cybernic master system is a master-slave system for manipulations and consists of master-slave robot arm and visual feedback system. The Cybernic master arm uses joint torque estimation method, based on Bioelectrical Signal. To reap full advantage of the control method, not only feedback to somatosensory system such as force and impedance control but also optimal visual feedback is an important factor in transmitting information to an operator. To achieve visual feedback, it is installed stereoscopic vision and operation assist system using Augmented Reality. The stereoscopic vision is controlled by our active control method of a convergence angle depending on the distance to objects. The operation assist system can show stereoscopic images that is overlaid the virtual objects. Using the virtual objects such as virtual walls and protected areas, it is possible to assist the safe operations. We conducted experiments to verify that the operator can view parallax image stereoscopically at the leaching range that is near to a human arm. Our system in short distance was effective compared with normal parallax method. Then, we conducted operation test to ensure that it is possible to perform the area protection with the virtual wall using our system. At the result, protection areas were formed, and we ensured that slave arm robot could not invade those areas. In addition, the operation assists such as not only protection of crash but also the tracing movement and operation instruction by the virtual walls is possible.

I. Introduction

THERE are dangerous tasks such as the dismantling of nuclear power plant and the high-level radioactive material handling. The extended activity on radioactive environment is a hazard to the human, so robots are necessary to work in place of it. However, it is difficult for the autonomous robots that cannot provide flexible service in diverse situations to perform the complex tasks. In order to directly manipulate remotely situated objects in such hazardous environments, master slave systems have been proposed. The research about master slave type manipulation system is performed in the field of robotics and the virtual reality. Representative example of the master slave systems provide tele-existence experiences [1]-[4].

To reflect human muscle properties in the robot arm for master slave systems, we developed the Cybernic master system and control method [2]. Our control method can voluntarily express robot arm impedance based on Bioelectrical Signal intensity, which is provided from the intuitive arm motion of the operator. Fig.1 shows the concept of Cybernic master system during manipulation. With the mechanical feedback, our system produces an augmented reality experience as if the operator is in a remote place while operating the target objects directly. When the operator manipulates a remotely situated object, the visual awareness of the environment is vital to control a state of slave arm robots. Therefore, not only feedback to somatosensory system such as force and impedance control but also optimal visual feedback is an important factor to transmit the information to the operator. In particular, 3D depth information is can be crucial when trying to accurately control a robotic arm using a remote display. Furthermore, displaying movement restriction information or visually enhancing an object in real time can greatly reduce the chance for mistakes for the remote operator.

In this study, we develop an augmented reality, 3D visual feedback system for Cybernic master system. The system consists of motion 3D Camera System to get information of working space and Operation Assist System to present visual information and avoid mistakes caused by false recognition. Fig.2 shows the configuration of 3D visual feedback system.

II. Material and Methods

A. Motion 3D Camera System

In order to operate remotely situated slave robotic arms in all 3 dimensions, it is important how the operator performs recognition of the depth information. When the operator going to operate it using a monocular camera, the technological problems may be stated as follows.

1) The operator cannot get depth information using a monocular camera. To get depth information, it is necessary to use the different angle cameras.
2) When using multiple cameras, the operator has to check the multiple simultaneous visual feeds on the monitors. This method contains the potential hazard of operation mistake.
3) It decreases operator's working efficiency when the operator must operate multiple cameras.

This study was supported in part by the Grant-in-Aid for the Global COE Program on Cybernics: fusion of human, machine, and information systems at the University of Tsukuba and relevant organizations.
Manuscript received October 10, 2012. Part of this work was supported by the "Funding Program for World-Leading innovation R&D on Science and Technology (FIRST Program)," initiated by the Council for Science and Technology Policy (CSTP).
Kousuke Hiramatsu is with Systems and Information Engineering, University of Tsukuba, Tsukuba, IBARAKI 3050006 Japan. (e-mail: hiramatsu@golem.kz.tsukuba.ac.jp).
Yoshiyuki Sankai is with Systems and Information Engineering, University of Tsukuba, Tsukuba, IBARAKI 3050006 Japan. (e-mail: sankai@golem.kz.tsukuba.ac.jp).

978-1-4673-1497-8/12/$31.00 ©2012 IEEE

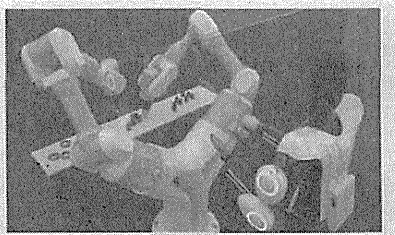

Fig. 1. This image is final concept of master-slave manipulation system. An operator manipulates a slave arm in work space with Cybernic master system.

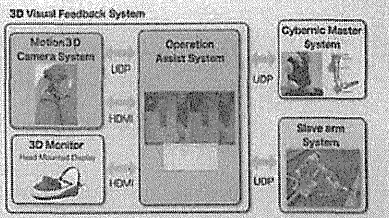

Fig. 2. The configuration of 3D visual feedback system. It consists of Motion 3D Camera System and Operation Assist System. Cybernic master system and slave arm system can communicate the system using UDP protocol.

To solve the above problems, the main specifications that are necessary for the motion 3D camera system are as follows.

1) To get parallax image, the system uses stereo camera (parallel method and cross method).
2) Using 3Axis motion platform and head tracking, the system performs handsfree camera control.
3) To adapt to stereoscopic vision at near distance, the system can perform active control of convergence angle.

Using stereo camera based stereo vision and head tracking based motion platform, the operator can recognize the working space more effectively than with conventional systems. However, when the manipulation is in the leaching range similar to the human arm, the operator cannot view parallax image accurately using only the parallel method. This is because the effect of convergence angle increases. Our system is installed with an active control mechanism of convergence angle depending on the distance to objects. In our system, the base length of the camera is the same as the distance of human eyes. Fig.3 shows the mechanism control method for the convergence angles of right camera and left camera based on the distance of the camera to a gaze object at the same time using an actuator. When the distance of the camera to the gaze object is measured, the convergence angle, α [rad], is calculated as

$$\alpha = tan^{-1}\frac{2a}{d} \tag{1}$$

where a[mm] and d[mm] are the distance of the camera to the gaze object and the base length of the stereo camera. An average base length of the human eyes of 58[mm] to 72[mm] has been reported [6]. In this study, we selected 65[mm] as the base length d [mm]. Using the convergence angle of α [rad] , the coordinate of point A , x[mm], y[mm], is calculated as

$$x = \frac{d}{2} + b\cos\alpha \tag{2}$$
$$y = f - b\sin\alpha \tag{3}$$

where b[mm] and f[mm] are the length of link. The

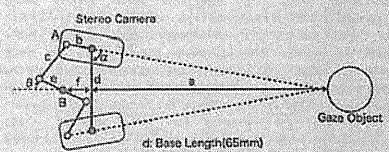

Fig. 3. This graphic is the mechanism of how to control the convergence angles of right camera and left camera based on the distance of camera to a gaze object at the same time using an actuator.

coordinate origin of Equation (2) - (3) is the point B.
The actuator angle, θ[rad], is calculated by:

$$\theta = \frac{\pi}{2} - \left\{cos^{-1}\left(\frac{x^2+y^2+e^2-c^2}{2e\sqrt{x^2+y^2}}\right) - tan^{-1}\left(\frac{y}{x}\right)\right\} \tag{4}$$

where e[mm] and c[mm] are the length of link. The actuator controls α [rad] of the convergence angle of cameras by turning link e.

When the distance to a gaze object was provided, the system can control the convergence angle of cameras using Equation (4). Also it is possible to focus the gaze point of camera on an object. In addition, the system can also use a self-regulation of the cameras about the focus alignment. The camera can focus it at 100[mm] from the lens. Using cross method that is active control of convergence angle, the operator can view parallax image stereoscopically at the leaching range that is near to a human arm about less than 1000[mm]. To measure the distance of camera to objects and automatically control the convergence angle, we use Position Sensitive Detector (PSD) sensor. An absolute angle sensor estimates the operator's head motion and posture.

To operate the view direction of our stereo camera depending on the operator's head motion, we develop 3axis

motion platform. After having measuring the operator's head motion using an absolute angle sensor, it estimates posture from the motion and transmits a data to motion platform.

Fig.4 shows the overview of motion 3D camera system. The system has a sensor to measure the distance to a gaze object, and controls convergence angle between a right camera and a left camera in 1 [kHz] sampling. Fig.5 shows the information flow of motion 3D camera system. Absolute angle sensor sends information of head motion to host computer using Bluetooth, and host computer sends absolute angle of operator's head to 3 axis motion platform using UDP protocol. 3 axis motion platform can control camera posture based on received data by actuators that is installed on roll, pitch and yaw axis.

B. Operation Assist System

The purpose of this operation assist system is not only to present stereoscopic images of working space to the operator but also to assist manipulation using 3D computer graphics (3DCG) creating an augmented reality visual feedback system. To improve efficiency of the operator's work, reducing operation mistakes and guiding the operator in the direction of objects is predictably-effective, as the operator should avoid accidents such as the collision of slave arm robots and the target objects. We develop the operation assist system, which can show the virtual wall using augmented reality technology. This virtual wall can stop movements of slave arm robots on the reality space. The main specifications that are necessary for the system are as follows:

1) Stereoscopic image is got from the stereo camera using High-Definition Multimedia Interface (HDMI) 1.4, and outputted to 3d monitor such as Head Mounted Display after generating side-by –side stereoscopic image overlaid real-time 3D CG images.
2) The posture of 3D camera system and virtual camera in the virtual space is synchronized.
3) Operation assist by interactive communication of CG object in virtual space and slave arm robots in real space is mounted.

Fig.6 shows the information flow of operation assist system. The operation assist system receives the information of the camera posture and the parallax images from motion 3D camera system. The stereoscopic image that was overlaid with 3DCG is outputted to 3D monitor. It is possible for the operator to watch stereoscopic view while operating the master arm system. At the same time, the master arm system transmits the information of the end effector. The operation assist system synchronizes the position of the CG objects and the position of the slave arm end effector based on the received information from the master arm system. Then, the end effectors in the reality space and the CG objects of the virtual space are equivalent, and this operation allows interaction. Moreover, we adopt the Axis Aligned Bounding Box (AABB) method [7] using the bounding boxes for the collision detection in the CG objects. To detect the collision, it is necessary to surround a slave arm end effector and the CG objects with bounding boxes. When a slave arm comes in contact with CG objects, the system revises the positional information from a master arm to no longer invade the area, and transmits it to a slave arm. In addition, physical characteristic such as mass, viscosity, and elasticity, is set to the each object in the virtual space. It can replicate the reactive force of the objects to the operator by sending back the position of end effector to the master system.

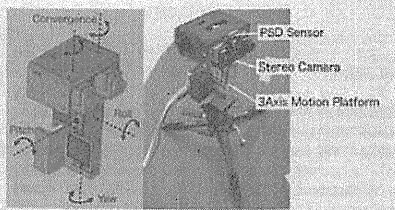

Fig. 4. The overview of motion 3D camera system. To measure the distance to gaze objects, it use the PSD sensor. The system has 3 degree of freedom and axis of convergence angle.

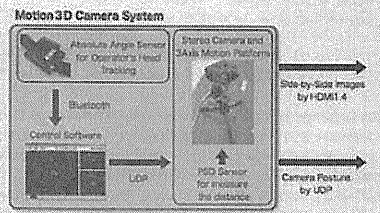

Fig. 5. The information flow of Motion 3D Camera System. It consists of stereo camera, 3axis motion platform and absolute angle sensor for operator's head tracking. 3axis motion platform can control the posture of stereo camera by operator's head motions. Then, that information is sent to operation assist system using UDP protocol.

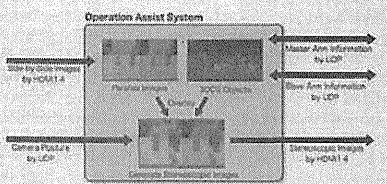

Fig. 6. The information flow of Operation Assist System. The system receives the information of the camera posture and parallax image from motion 3D camera system. Stereoscopic images are generated using camera posture and 3DCG objects. Then, those images are sent to 3D monitor using HDMI. In addition, position of end effector is send to master system and slave system using UDP protocol.

III. Experiments

The developed 3d visual feedback system based on our control method was confirmed through operation experiments.

Fig. 7 shows the appearance of the tests. The test circumstance was constructed with a slave arm, Cybernic master arm, the target objects, and the 3d visual feedback system. The operator used the Cybernic master system in order to operate the slave arm. Our camera system was fixed to the place such that the slave arm looked like the operator's own arm.

A. Operation check of the camera system

In order to ensure the operation of the developed system, the following three validations were carried out.

1) Synchronization operation of the camera system:: Synchronization operation of the camera posture was evaluated by an experiment. The head tracking sensor was worn the operator. The head of the operator could move about freely. The control software was connected with the head tracking sensor using Bluetooth. Motion 3D camera system was connected with the control software using UDP protocol. In addition, the head tracking sensor had its zero point calibrated to the front-facing position of the operator.

2) Convergence angle control verification:: We conducted the experiments to ensure that the system could operate the convergence angle of the camera automatically based on the distance of the gaze object. The position and posture of the camera was fixed, and the target object was placed in the front of the camera at different positions.

B. Effectiveness of the convergence angle control

Effectiveness of the convergence angle control was demonstrated by using 11 subjects. In particular, it was important that the subjects could get out of the stereoscopic as the depth information. It was necessary to perform the comparative experiments within 1000[mm] of an arm leaching area. Following two comparisons were carried out.

1) Comparison of stereoscopic area:: We conducted the comparative experiments to ensure that the operator could view the stereoscopic vision using the system based on our method and the normal parallel method that was fixed the convergence angle. The subjects could view the stereoscopic images by the head mounted display. The measurement area was 1000[mm] to 100[mm] in front of the camera. In the area, the gaze objects was moved randomly every 100[mm].

2) Comparison of viewability:: We verified if it is easy to the stereoscopic vision using the system based on our method and the normal parallel method. The subjects should vote for the method that stereoscopic vision was made faster. The other method of the experiment was similar to experiment *1)*.

C. Validation of operation assistance

To improve efficiency of the operator's work, an augmented reality based operation assist system was composed for assisting the operation. The usability of the system for reducing the operation mistakes was validated.

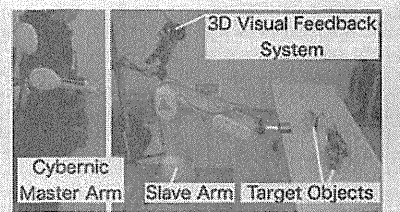

Fig. 7. This image shows the appearance of the tests. The test circumstance was constructed with a slave arm, Cybernic master arm, the target objects, and the 3d visual feedback system.

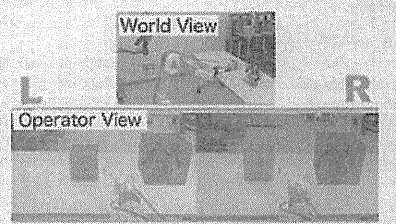

Fig. 8. This image shows the screen of operation assist system in the operation. The operator views right and left parallax images overlaid match move 3DCG information at real world

Fig.8 shows the screen of operation assist system while operating the master arm system. The operator was checking the stereoscopic images using the head mounted display, while operating the master system. Following two validations were carried out.

1) Implementation of the object protection:: We conducted the experiment to ensure that the bounding boxes could provide for the protected objects. The protected objects and table were placed on the front of the slave arm. Motion 3d camera system was fixed to the place quite same as the viewpoint of the operator. We sketched the bounding boxes for objects and table, and adjusted viewpoint of virtual reality camera. Position and distance between a slave arm robot and objects were given. The operator controlled a slave arm robot to try to reach the protected objects.

2) Implementation of the operation guide:: We conducted the experiment to ensure that the virtual walls could guide for the operation. The virtual walls had the properties similar to the protected objects. The target object and table ware placed on the front of the slave arm. In addition, the virtual walls surrounded the approach line to the object. The operator controlled a slave arm robot to try to reach the object.

IV. Results

A. Operation check of the camera system

1) Synchronization operation of the camera system:: We verified whether the synchronize operation of the camera

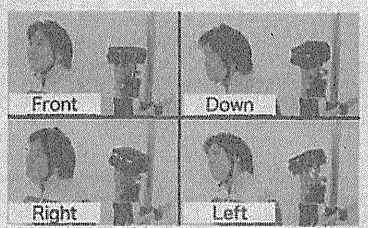

Fig. 9. This image shows the result of the operation about the camera posture. The camera posture was moved in synchronization by the operator's head motion.

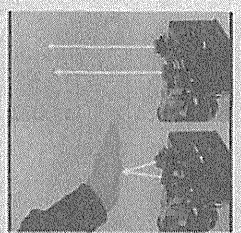

Fig. 10. The overview of the convergence angle control. When gaze object approach the camera, it is possible to control the convergence angle depending on the distance to the object.

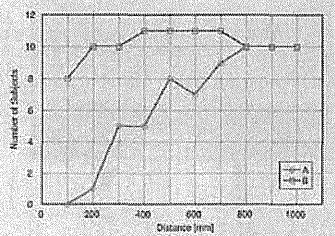

Fig. 11. This chart shows the number of subjects that can view the stereoscopic. Line *A* is result of normal parallel method and line *B* is result of our cross method based on active control of convergence angle.

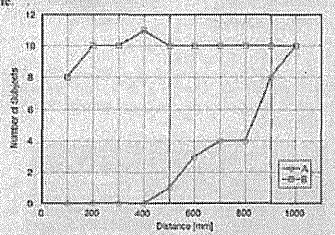

Fig. 12. This chart shows the number of subjects that scan view the stereoscopic vision faster. Line *A* is result of normal parallel method and line *B* is result of our cross method based on active control of convergence angle.

system. Fig.9 shows the result of the operation about the camera posture. The camera posture was moved in synchronization by the operator's head motion.

2) Convergence angle control verification:: We verified whether the system could operate the convergence angle of the camera automatically based on the distance of the gaze object. Fig.10 shows the result of the active control for the convergence angle. The angle of the camera was able to change based on our method.

B. Effectiveness of the convergence angle control

1) Comparison of stereoscopic area:: Fig.11 shows the result of the comparison of stereoscopic area. In Fig.11, line *A* is result of normal parallel method and line *B* is result of our method based on active control of convergence angle. As a result, in our method, there are many numbers of subjects that are stereoscopic vision possibility in distance less than 600[mm] ~ 700[mm] compared with normal parallel method. Moreover, stereoscopic vision is difficult in the normal parallel method for the ranges of 100[mm] ~ 200[mm], but it is possible using our method.

2) Comparison of viewability:: Fig.12 shows the result of the comparison of viewability. In Fig.12, line *A* is result of normal parallel method and line *B* is result of our method based on active control of convergence angle. Our method is easier to view stereoscopic image than normal parallel method in the whole area of 100[mm] ~ 1000[mm].

C. Validation of operation assistance

1) Implementation of the object protection:: Fig.13 shows the trajectory of slave arm end effector when the bounding boxes were placed to surround the protected objects. The trajectory that was formed surrounding the protected objects. As the result, protection areas were formed, and we ensured that slave arm robot could not invade those areas. Because of that, protected objects and slave arm robot did not collide physically. The slave arm end effector of the reality space is subject to the limitation of the movement by coming in contact with the objects of the virtual space. However, unlike contact of the reality space, the physical damage does not occur to a slave arm because it is only the collision detection in the virtual space. Furthermore, the protection object of the reality space can avoid the critical contact with the slave arm because the protection object of the virtual space protects it.

2) Implementation of the operation guide:: We evaluated whether it was possible for an operation guide by the tracing movement using the virtual walls. Fig.14 shows the virtual walls and the trajectory of slave arm end effector in the tracing movement. The virtual walls were made by a method same as protection area generation using bounding boxes.

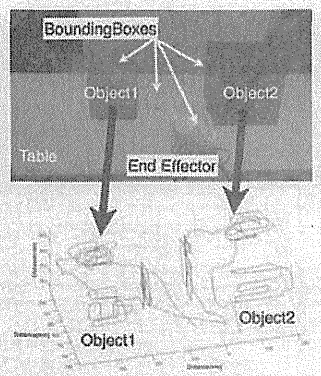

Fig. 13. This image shows the trajectory of slave arm end effector when the bounding boxes were placed to surround the protected objects. There is the trajectory that was formed surround the protected objects1 and object2.

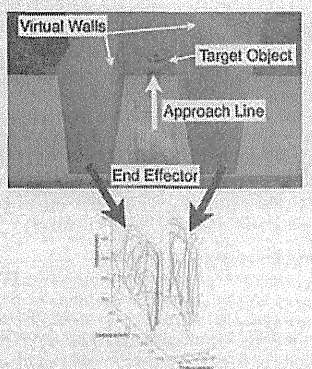

Fig. 14. This image shows the virtual walls and the trajectory of slave arm end effector in the tracing movement. There is the trajectory that was formed surround the virtual walls.

The trajectory is produced along virtual walls. The operator could operate the slave arm in the limited area, which was surrounded by the virtual walls. It was possible for the slave arm to only move the target object without coming in contact with the surround objects in the reality world.

V. Discussion

When using a master slave system, it is important to perform visual feedback. In this study, to improve efficiency of the operator's work, we developed the 3D visual feedback system.

As a result of experiment B, we verified the effectiveness of the convergence angle based on our method. Then, stereoscopic vision is difficult in the normal parallel method in 100[mm] ~ 200[mm], but it is possible by our method. In area of near the camera, it is thought that it is difficult for human to view the stereoscopic image that is got by normal parallel method, because the influence of the convergence angle appears conspicuously at the 65[mm] base length and the gap of parallax image is larger. By contrast, using our method, subjects can view the parallax image that is controlled convergence angle and the gap of parallax similar to human eyes. Using our method that is active control of convergence angle, we conducted these experiments to ensure that the operator can view parallax image stereoscopically at the leaching range that is similar to the human arm about less than 1000[mm].

As a result of experiment C, we verified the operation assist using developed system. It thought that it reduces the input agitation of the operator and the crash by operating a slave arm, while tracing virtual walls to the target objects. Furthermore, when the complex task requires high concentration, the operator can be less concerned with surroundings of the slave arm. The placement of the virtual walls and the reaction force they produce also help with the guidance of the robotic arm, increasing usability. So, we can anticipate improvement of the operation efficiency.

VI. Conclusion

In this study, to achieve 3D visual feedback system for Cybernic master system, we developed motion 3D camera system, which is installed active control mechanism of convergence angle depending on the distance to objects, and installed 3axis motion platform. In addition, we developed the operation assist system, which can show stereoscopic image and the virtual objects. It is thought that to achieve the interaction between the object of the virtual space and an object of the reality space is very significant in our developed system.

References

[1] Susumu Tachi, Taisuke Sakaki, Hirohiko Arai, Shoichiro Nishizawa and Jose F. Pelaez-Polo,"Impedance Control of a Direct-drive Advanced Manipulator without Using Force Sensors",Advanced Robotics, Vol.5, No.2 (1991),4,pp.183-205.

[2] S.Tachi, T.Sakaki,"Impedance controlled master-slave manipulation system Part1 Basic concept and application to the system with a time delay",Advanced Robotics,Vol.6,No.4 (1992),pp.483-503.

[3] R.Tadakuma, K.Sogen, H.Kajimoto, N.Kawakami and S.Tachi,"Development of Multi-D.O.F. Master-Slave Arm with Bilateral Impedance Control for Telexistence", Proceedings of the 2004 International Sympojium on Measurement, Control, and Robots,(2004).

[4] I.Yamano K.Takemura K.Endo T.Maeno,"Method for Controlling Master-Slave Robots using Switching and Elastic Elements",Proceedings of the 2002 IEEE International Conference on Robotics & Automation, (2002),pp.1717-1722.

[5] Kousuke Hiramatsu, Yoshiyuki Sankai,"Proposal for Manipulation System with Cybernic Master Arm based on BES Variable Impedance Control", The Japan Society of Mechanical Engineers, Serias C, Vol.77, No.784, pp 330-239 (2011).

[6] Thompson P., "Eyes wide apart: Overestimating inter-pupillary distance", Perception, Vol. 31(6), pp.651 – 656, 2002.

[7] P. JimeH nez, F. Thomas, C. Torras, "3D collision detection: a survey",Computers & Graphics, Vol. 25, Issue 2, pp. 269–285(2001)

2012 IEEE/SICE International Symposium on System Integration (SII)
Kyushu University, Fukuoka, Japan
December 16-18, 2012

Stair Ascent assistance for Cerebral Palsy with Robot Suit HAL

Takumi Taketomi and Yoshiyuki Sankai

***Abstract*—Cerebral palsy (CP) patients require a wheelchair for moving when their lower limbs are severely paralyzed. Wheelchair users have issues moving around due to the lack of optimal infrastructure. We achieved a voluntary walking of a CP patient who uses wheelchair by using our developed hybrid assistive limb (HAL). In addition to voluntary walking, if HAL realizes voluntary stair climbing, it is expected that patients will acquire a wider range of activities than using a wheelchair. This study focuses on stair ascent. The purpose of this study is to propose an automatic control method for stair ascent assistance, and to verify the effectiveness of the proposed method. In this method, a phase of stair ascent is determined by proposed phase determination based on a height of landing area, CoGRF in sagittal plane and lateral plane. Proposed automatic control generates torque for assisting each phase movement during stair ascent. As an experiment, healthy male subject went through a course including flat area and stairs. As a result, we verified that the phase determination could determine the phase during stair ascent and switch between the walking assistance method and stair ascent assistance method. The proposed automatic control generated torque for assisting movement of each phase. We found this proposed method is applicable to for walking and stair ascent assistance.**

I. Introduction

CEREBRAL Palsy (CP) is one of mobility disorders caused by brain damage. Eighty-eight percent of CP patients have spastic [1]. Spastic is divided into 3 groups by paralysis part, hemiplegia, paraplegia and quadriplegia. Paraplegia and quadriplegia patients get paralyzed in their lower limb [2]. When their lower limbs are severely paralyzed, they require a wheelchair for moving. Wheelchair users have issues moving around due to the lack of optimal infrastructure. To acquire the range of their activities, the realization of voluntary walking and stair climbing are extremely important.

We have developed the robot suit Hybrid Assistive Limb (HAL), a cyborg-type robot that can expand and improve human physical capability [3]-[5]. In Previous study, a walking assistance method for a quadriplegia patient was proposed. The proposed method consists of two algorithms. Those are an assistance of voluntary movement in the swing phase and an automatic assistance of weight bearing in the stance phase and gravity compensation in swing phase [5]. As shown in Fig. 1, the method achieved voluntary walking of a subject who could not walk himself. In addition to voluntary walking, if HAL realizes voluntary stair climbing, it is expected that patient will acquire a wider range of activities than using wheelchair. This study focuses on stair ascent.

The purpose of this study is to propose an automatic control method for stair ascent assistance, and to verify the effectiveness of the proposed method.

Manuscript received September 21, 2012. Part of this work was supported by the "Funding Program for World-Leading Innovative R&D on Science and Technology (FIRST Program)," initiated by the Council for Science and Technology Policy (CSTP).

All the authors are with Cybernics Laboratory, Systems and Information Engineering, University of Tsukuba, Ibaraki 305-8573, Japan (e-mail: taketomi@golem.kz.tsukuba.ac.jp; sankai@golem.tsukuba.ac.jp).

II. Phase Determination

In previous study, an automatic control method for walking assistance with HAL was proposed. The method consists of two algorithms, that is, gravity compensation in the swing phase, and assistance of weight bearing in the stance phase. The method divided walking cycle into three phases, $L_{st}R_{sw}$, in that phase, the left leg is stance leg and the right leg is swing leg, D_{st}, in that phase, the left leg and the right leg are stance leg and $L_{sw}R_{st}$, in that phase, the left leg is swing leg and the right leg is stance leg. The phase determination method for walking assistance determines the phase based on center of ground reaction force (CoGRF) in lateral plane. As shown in Fig. 2, in the phase determination, stance leg polygon is defined as a rectangle that is made up from four representative floor reaction force (FRF) measuring points.

In that definition, CoGRF in lateral plane calculated as follows.

$$C_x = \frac{f_{tr} + f_{hr}}{f_{tl} + f_{hl} + f_{tr} + f_{hr}} \tag{1}$$

where C_x is CoGRF in lateral plane; f_{tr} is FRF measured at right toe; f_{hr} is FRF measured at right heel; f_{tl} is FRF measured at left toe and f_{hl} is FRF measured at left heel.

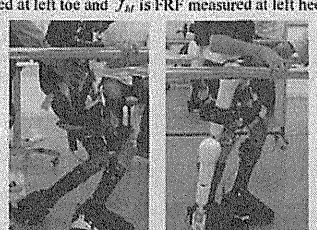

Fig. 1. Realization of voluntary walking. Walking without HAL (left). Walking with HAL (Right). Without HAL, subject could not stand himself. Though, he could walk himself by using HAL.

(2) is phases and those predefined thresholds.

$$Phase = \begin{cases} L_{st}R_{sw} & (C_x < (1 - C_{x\_th})) \\ D_{st} & ((1 - C_{x\_th}) \le C_x \le C_{x\_th}) \\ L_{sw}R_{st} & (C_{x\_th} < C_x) \end{cases} \tag{2}$$

where *Phase* is a present phase and C_{x_th} is predefined threshold point of CoGRF in lateral plane.

When *Phase* transits, assist control switches. The method realized voluntary walking of a subject who could not walk himself.

Unlike normal walking, during stair ascent, swing leg landed on an upper step. As shown Fig. 3, when the landed foot is incompletely touched the step, assume that the polygon is smaller than the area of the sole of the foot. In that case, the phase determination will determine incorrectly the transition from D_{st} to $L_{st}R_{sw}$ or $L_{sw}R_{st}$ on upper step.

Therefore, to determine the phase transition in stair ascent, we propose a phase determination method that is based on height of a landing area, CoGRF of lateral plane, and CoGRF of sagittal plane.

A. Phase Determination based on height of landing area

The proposed phase determination method for stair ascent defines the height as the height from the left ankle to the right ankle. Fig. 4 shows definition of system parameters and variables. Since the height from the step to each ankle is even, the defined height is the same as the height of the step during D_{st}. The height is calculated as follows.

$$\begin{aligned} h = {} & l_{thigh}\cos(\theta_{abx} - \theta_{hr}) + l_{shank}\cos(\theta_{hr} + \theta_{abx} - \theta_{kr}) \\ & - l_{thigh}\cos(\theta_{abx} - \theta_{hl}) - l_{shank}\cos(\theta_{hl} + \theta_{abx} - \theta_{kl}) \end{aligned} \tag{3}$$

where h [m] is the height from the left ankle to the right ankle; l_{thigh} [m] is the length of the thigh; l_{shank} [m] is the length of the shank; θ_{abx} [rad] is the absolute angle of the trunk; θ_{hr} [rad] is the angle of the right hip; θ_{kr} [rad] is the angle of the right knee; θ_{hl} [rad] is the angle of the left hip and θ_{kl} [rad] is the angle of the left knee.

The height of landing area is calculated by using (3) at the moment of the phase was transited from a single stance phase to double stance phase. When the height exceeds the predefined threshold, the phase determination determines wearer is climbing up stairs.

B. CoGRF-based Phase determination

The CoGRF-based phase determination has a prerequisite condition, that is, all of representative FRF measuring points are on steps. When the FRF value exceeds a predefined threshold as shown in (4), the determination determines landing.

$$\begin{cases} f_{rh} > f_{th} & (Phase = L_{st}R_{sw}) \\ f_{lh} > f_{th} & (Phase = L_{sw}R_{st}) \end{cases} \tag{4}$$

where f_{th} is a predefined threshold value of FRF.

CoGRF in sagittal plane in the stance leg polygon defined by the previous study is calculated as follows.

$$C_y = \frac{f_{hr} + f_{tr}}{f_{tl} + f_{hl} + f_{tr} + f_{hr}} \tag{5}$$

where C_y is CoGRF in sagittal plane.

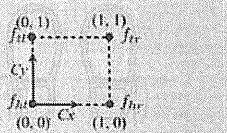

Fig. 2. The definition of stance leg polygon and the coordinate system of CoGRF in the phase determination for walking assistance. Stance leg polygon is defined as a rectangle that is made up from four representative floor reaction force (FRF) measuring points.

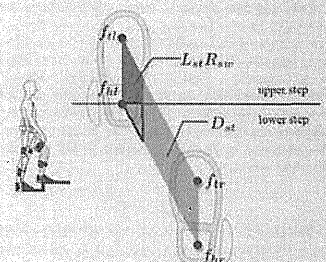

Fig. 3. Example of the incompletely landed foot. When CoGRF in the gray area, the phase is D_{st}. After CoGRF moves in dark gray area, the phase turns into $L_{st}R_{sw}$. The phase determination will determine the phase $L_{st}R_{sw}$ or $L_{sw}R_{st}$ regardless of the phase is D_{st}. The incorrect determination will occur when CoGRF is in the boxed area.

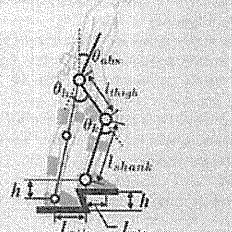

Fig. 4. Definition of system parameters and variables. The flexion direction of each joint angle is set to be positive and each joint angle becomes 0 [rad] in upright posture.

A stride is defined as distance between ankles that is calculated as follows.

978-1-4673-1497-8/12/$31.00 ©2012 IEEE

$$l_{stride} = l_{thigh}\sin(\theta_{abs}-\theta_{hr}) + l_{shank}\sin(\theta_{kr}+\theta_{abs}-\theta_{hr}) - l_{thigh}\sin(\theta_{abs}-\theta_{hl}) - l_{shank}\sin(\theta_{kl}+\theta_{abs}-\theta_{hl}) \quad (6)$$

where l_{stride} is a defined stride.

Fig. 5 shows the coordinate system of CoGRF when legs are placed back and forth. This coordinate system is different from the coordinate system shown in Fig. 2. That is, the representative FRF measuring point of a toe of the back side leg, and representative FRF measuring point of a heel of the forth side leg are placed at different points from the points on the coordinate system shown in Fig. 2. In that coordinate system, CoGRF in sagittal plane is calculated as follows.

$$C_y = \begin{cases} \dfrac{|l_{stride}|C_x + l_{sole}C_y}{|l_{stride}| + l_{sole}} & (l_{stride} \geq 0) \\ \dfrac{|l_{stride}|(1-C_x) + l_{sole}C_y}{|l_{stride}| + l_{sole}} & (l_{stride} < 0) \end{cases} \quad (7)$$

where C_y is CoGRF in sagittal plane when legs are placed back and forth; l_{sole} is the length of the sole which is defined as the distance between representative FRF measuring points of heel and toe in the same sole.

In the sagittal plane, the threshold which determines whether CoGRF is in the single leg stance leg polygon or not is defined as follows.

$$C_y > \frac{|l_{stride}|}{l_{sole} + |l_{stride}|} \quad (8)$$

Proposed phase determination for stair ascent uses (8), and the threshold of CoGRF in lateral plane that is the same as walking assistance. Fig. 6 shows the follow chart of the phase determination. The phase determination determines three phases in stair ascent, that is, $L_{st}R_{sw}$, D_{st} and $L_{sw}R_{st}$. When the height of landing area is lower than the height of a step, the determination determines that wearer is walking.

III. Automatic Control For Stair Ascent Assistance

In stair ascent, movements of wearer are different between phases. In swing phase, joints of the swing leg are flexed voluntarily to land the foot on the upper step. In double stance phase, joints of the leg on the lower step are extended to keep the leg in extended position for weight bearing, and joints of the leg on the upper step are flexed to move the CoGRF into the stance leg polygon of upper leg. In single stance phase, the hip joint is rotated to keep the CoGRF in the supporting leg polygon, and the knee joint is extended to lift up the body [6].

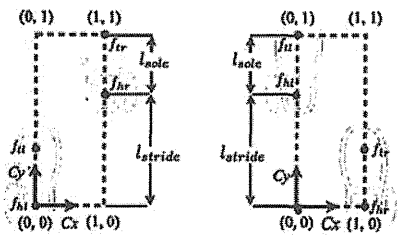

Fig. 5. The coordinate system of CoGRF when legs are placed back and forth. When left leg is forth (Left). When right leg is forth (Right). This coordinate system is different from the coordinate system shown in Fig. 2. That is, the representative FRF measuring point of a toe of the back side leg, and representative FRF measuring point of a heel of the forth side leg are placed at different points from the points on the coordinate system shown in Fig. 2.

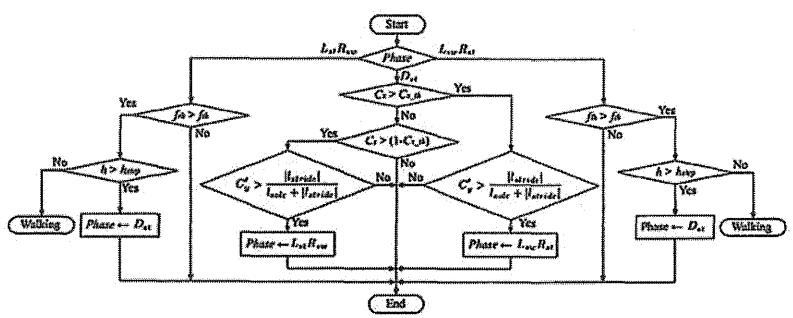

Fig. 6. The follow chart of the phase determination for stair ascent. Where h_{step} is the predefined height of a step; "Walking" means the control method is switched into walking assistance.

We propose an automatic control method for assisting stair ascent, which is based on the movement of each phase. The method consists of three algorithms: gravity compensation in the swing phase, assistance of weight bearing in the double stance phase and assistance of upward movement in the single stance phase.

The movement of swing leg and the movement of stance leg on the lower step are the same as in walking. Thus, gravity compensation and assistance of weight bearing proposed in previous study could be used for these movements. In this method, we propose an automatic control for assisting upward movement in the single stance phase.

When wearer moves upward, a following load is applied to the knee joint

$$W = \begin{cases} (1-C_x)M & (Phase = L_{st}R_{sw}) \\ C_xM & (Phase = L_{sw}R_{st}) \end{cases} \quad (9)$$

where W is applied load to the knee joint; M is the weight of the wearer.

To lift wearer's body up, flowing knee joint torque is generated.

$$\tau_k = Wgl \quad (10)$$

where τ_k is generated knee joint torque; g is acceleration of gravity; l is distance between knee joint and center of gravity (COG) in sagittal plane.

As shown in Fig. 7, the force vector from the COG and the force vector from the CoGRF are placed at the same point [7].

Thus, in single stance phase, l is defined as distance between CoGRF in sagittal plane and knee joint.

In that case, knee joint torque τ_k is calculated as

$$\tau_k = Wg\{l_{shank}\sin(\theta_k + \theta_{abs} - \theta_h) - (l_{sole} + |l_{stride}|)C_y + |l_{stride}|\} \quad (11)$$

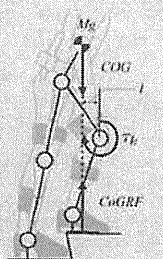

Fig. 7. The force vector from the COG and the force vector from CoGRF during moving upward. These vectors is considered to be in the same distance from the knee joint in the sagittal plane.

Proposed assistance of upward movement generates knee joint torque as follows.

$$\tau_{up} = G_{up}\tau_k \quad (12)$$

where τ_{up} is automatic generated torque for an upward movement assistance, G_{up} is the gain that adjusts the torque based on the body function of wearer.

IV. Experiments

An automatic control of the HAL for stair ascent assistance based on the proposed method was verified by experiments on flat area and stairs. Fig. 8 shows the environment of experiment. A step of the stair was 12 [cm] high, 72 [cm] wide, and a depth of 27 [cm].

The subject is a healthy male, 65 [kg] in weight, 166 [cm] in height, and the shoes size is 27 [cm]. The subject started walking voluntarily from 1.5 [m] away from the stairs. When arrived in front of the stairs, the subject started stair ascent. By this experiment, the validity of following three methods is examined.

A. Phase determination based on height of landing areas

The subject moved over flat area during walking and climbed up stairs during stair ascent. The proposed method was verified by comparing the heights of landing areas between walking and stair ascent. The Comparison is done by determining the significance difference using t-test. The heights were defined as the calculated height by using (2) at the moment of the phase was transited from a single stance phase to double stance phase.

B. CoGRF-based Phase determination

The phase was transited from double stance phase to single stance phase when CoGRF was in the stance leg polygon of the next single stance leg. The proposed method was verified by tracking the trajectory of CoGRF during the experiments. The trajectory was calculated based on the landed area of a stance leg.

Fig. 8. Environment of experiment. The stair was used for rehabilitation training. For the safety of the subject, touching the handrail was allowed. Though, using the handrail to move upward was not allowed.

A landed area of stance leg was defined as the position at the moment when the phase was transited from a single stance phase to double stance phase. It is the same value as the distance from the starting point of the movement. And

can be obtained by integrating absolute value of I_{stride}.

C. Automatic Control For Stair Ascent Assistance

The proposed automatic control generated torque for assisting movement of each phase. The effectiveness is examined by measuring the transition between calculated torque (8) and commanded torque.

V. Result

A. Phase determination based on height of landing areas

We verified the phase determination. Fig. 9 shows transition of h during the experiment. Points in Fig. 9 shows the heights of landing areas. Table 1 shows mean values and valiances of the heights of landing areas during walking and stair ascent. P-value is calculated by t-test. The heights of landing areas during stair ascent are significantly higher than during walking.

B. CoGRF-based Phase determination

We verified the phase determination. Fig. 10 shows landed areas and the trajectory of CoGRF with time from 17.5 [s] to 19.5 [s]. Dashed lines show the thresholds to determine the phase based on CoGRF. Boxed areas in Fig. 10 shows the areas, that is, phase determination based on only CoGRF in lateral plane could not determine the correct phase. The trajectory of CoGRF was gone through the area.

C. Automatic Control For Stair Ascent Assistance

We verified the validity of assist torque. Fig. 11 shows transition of the generated torque and the calculated torque by (8) of right knee joint with time from 17.5 [s] to 19.5 [s]. During assisting upward movement, maximum commanded extension torque was measured. That was 39.4 [Nm]. The proposed method switched the upward movement assistance to the weight-bearing assistance when required torque for upward movement assistance was less than limited torque for weight-bearing assistance.

VI. Discussion

A range of activity is considered to be closely related to activity of daily living ability levels [8].

As a result of experiment, we verified that our proposed method generated appropriately assist for each movement phases. It indicates that, the method is applicable for walking and stair ascent assistance.

TABLE 1
MEAN VALUES AND VALIANCES OF THE HEIGHTS OF LANDING AREAS

Walking	Stair ascent	P-value
0.0440 ± 0.012	0.122 ± 0.006	$p < 0.001$

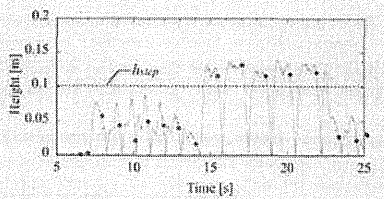

Fig. 9. Transition of h during the experiment. Points in the figure show the heights of landing areas. The heights of landing areas during stair ascent are significantly higher than during walking.

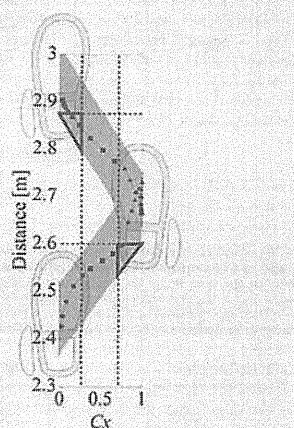

Fig. 10. Landing areas and the trajectory of CoGRF with time from 17.5 [s] to 19.5 [s]. Circle points show the CoGRF during $L_{st}R_{sw}$, rectangle points show the CoGRF during D_{st} and triangle points show the CoGRF during $L_{sw}R_{st}$. The gray area shows the defined stance leg polygon. Boxed areas shows the areas, that is, phase determination based on only CoGRF in lateral plane could not determine the correctly phase. Dashed lines show the threshold to determine the phase based on CoGRF.

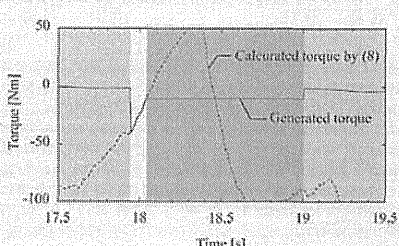

Fig. 11. Transition of the generated torque and the calculated torque by (8) of right knee joint with time from 17.5 [s] to 19.5 [s]. Generated torque for upward movement assistance is in white area, for gravity compensation is in gray area, and for weight bearing assistance is in dark gray area.

The assistance is expected to present effectual movement and sensory stimulation, those are considered to augment brain plasticity and enhance motor function. Several studies verified that training with that information presented from a robot enhanced motor function of a subject [9-12]. In addition, it was reported that voluntary movement promotes brain plasticity [13]. Therefore, we expect that he could acquire a wider range of activities than using wheelchair. Furthermore, by simply repeating using it, the patients' moving ability that is commonly considered being difficult to be enhanced, will be effectively improved.

Though we performed the experiment with a healthy male subject, clinical trials should be performed for application of moving assistance for CP patients. Because it was expected that he adjusted a movement involuntary. He could not completely mimic the movement of a CP patient. And, for assisting daily movement, stair descent assistance should be developed. When HAL could assist daily movement of CP, they will be able to move to anywhere.

VII. Conclusion

In this study, we proposed an automatic control method for stair ascent assistance, and verified the effectiveness of the proposed method. To determine phase transition in stair ascent, we proposed a phase determination method based on height of a landing area, CoGRF of lateral plane and CoGRF of sagittal plane. Our proposed automatic control method assists the motion of each phase. Experimental results showed the method was applicable for assisting walking and stair ascent. In the experiments, the method could determine the phase and generated torque for appropriate movement assistance of each phase during stair ascent. The phase determination could also determine the height of a landing area and switch the control into walking assistance seamlessly. This movement assistance method would help to acquire the range of activity of CP patients.

References

[1] KRÄGELOH-MANN I, CANS C., "Cerebral palsy update", *Brain & development*, vol. 31, no. 7, 2009, pp.537–544.

[2] C. Van den BROECK, J. DECAT, G. MOLENAERS, I. FRANKI, E. HIMPENS, D. SEVERIJNS, K. DESLOOVERE, "The effect of individually defined physiotherapy in children with cerebral palsy (CP)", *Eur. J. Paed. Neurol.*, vol. 30, 2010, pp.1–7.

[3] H. Kawamoto, Y. Sankai, "Power Assist System HAL-3 for Gait Disorder Person", in *Proc. of the 2002 Int. Conf. on Computers Helping People with Special Needs (ICCHP 2002)*, 2002, pp.196-203

[4] T. Hayashi, H. Kawamoto, Y. Sankai, "Control Method of RobotSuitHAL working as Operator's Muscleusing Biological and Dynamical Information", in *Proc. of IEEE/RSJ Int. Conf. on Intelligent Robots and Systems*, 2005, pp.3455-3460

[5] T. Taketomi, Y. Sankai, "Walking Assistance for Cerebral Palsy with Robot Suit HAL", *Trans Jpn Soc Med Biol Eng*, vol. 50, no. 1, 2012, pp. 105-11. (In Japanese with English abstract)

[6] A. Protopapadaki, WL Drechsler, MC. Cramp, FJ. Coutts and OM. Scott, "Hip, knee, ankle kinematics and kinetics during stair ascent and descent in healthy young individuals", *Clin Biomech (Bristol, Avon)*, vol. 22, 2007, pp.203–210

[7] L Mouchnino, ML Mille, M Cincera, A Bardot, A Delarque, A Pedotti and J Massion, "Postural reorganization of weight-shifting in below-knee amputees during leg raising", *Ex- perimental Brain Research*, vol. 121, 1998, pp. 205-214

[8] Tsuchiya K, Imada H, Okawa T, "Activities of daily living", Ishiyaku Publishers, 1992 (In Japanese)

[9] A. Meyer-Heim, I. Borggraefe, C. Ammann-Reiffer, S. Berweck et al., "Feasibility of robotic-assisted locomotor training in children with central gait impairment", *Dev Med Child Neurol*, vol. 49, 2007, pp. 900–906

[10] I. Borggrafe, A. Meyer-Heim, A. Kumar, J. Simon Schafer, S. Berweck, F. Heinen, "Improved gait parameters after robotic- assisted locomotor treadmill therapy in 6-year old child with cerebral palsy", *Mov. Disor.*, vol.23, no. 2, 2008, pp.280–283

[11] Golomb, M., et al., "In-home virtual reality videogame telerehabilitation in adolescents with hemiplegic cerebral palsy", *Arch Phys Med Rehabil*, vol. 91, 2010, pp. 1-8.e1.

[12] H.I. Krebs, B. Ladenheim, C. Hippolyte, L. Monterroso, J. Mast, "Robot-assisted task-specific training in cerebral palsy", *Developmental Medicine and Child Neurology*, vol. 51, 2009, pp.140-145

[13] F. Gómez-Pinilla, Z. Ying, R. R. Roy, R. Molteni, and V. R. Edgerton, "Voluntary exercise induces a BDNF-mediated mechanism that promotes neuroplasticity", *Journal of Neurophysiology*, vol. 88, 2002, pp.2187-2195

2012 IEEE/SICE International Symposium on System Integration (SII)
Kyushu University, Fukuoka, Japan
December 16-18, 2012

Visual Feedback System Showing Loads on Handrails for Gait Training

Ryotaro Sabe, Tomohiro Hayashi, Yoshiyuki Sankai

Abstract—**Patients with walking difficulties need support devices such as a walker or a cane. However, the support devices sometimes restrict their activities of daily living (ADL). In order to improve the patients' ADL, it is desired that they use the support device that does not restrict their activities as much as possible. The patients need gait training to reduce the dependence on the support device and to switch to a device with fewer restrictions. The purpose of this study is to develop a new visual feedback system that helps the patient receiving gait training to recognize their dependence on the support device. The developed system measures the load that the trainees applied on the handrails, and shows this load graphically by using a display monitor. The walking experiment was carried out with able-bodied subjects in order to ensure that the developed system can give the load feedback to the subjects and they could control the loads on handrails. The experiment was performed in the two cases in which the load information was shown to the subjects, and the load information was not shown to them. During the experiment, the subjects were instructed to adjust the load in accordance with the reference load indicated by the graphical user interface of the developed system. As a result, the subjects could adjust the load to the reference load more appropriately when the load information was given to them. The result, therefore, suggests that the developed system is able to help trainees to be aware of and control the load supported by their arms.**

I. Introduction

Walking is an important part of the activities of daily living (ADL). The patients with walking difficulty need support devices such as walkers or canes to maintain their posture and support their body weight instead of their impaired lower limb. With the help of the support device, the patients can improve their ADL. However, the support device sometimes also restricts their common daily activities. In order to improve the patients' ADL effectively, it is desired that they use the support device that does not restrict their activities as much as possible. The patients need gait training to reduce the dependence on the support device and to switch to a device with fewer restrictions. If the patients can reduce the loads applied on the handrails of support devices from their upper limbs, the dependence on support devices can be reduced. Therefore, it is important for the patients to practice walking in an effort to reduce the loads on the handrails, and switch support devices from such as walkers to canes as shown in Fig. 1.

For the gait training, the trainees need to know whether their body movement is appropriate or not. Commonly, trainers such as a physical therapist (PT) observe the trainee's movement and teach them to walk appropriately. Some information on the body movement, however, is difficult to assess correctly by the observation. Moreover, such information is also difficult to show quantitatively to the trainees verbally. To solve these problems, there are a lot of systems that give a feedback to the trainees [1]-[8]. However, to the best of our knowledge, there is no visual feedback system that can measure the loads on handrails and show them to the trainees objectively in the actual training scene. If such kind of system is developed, it would help patients to reduce the degree of dependence effectively and help them to switch the support devices to that with fewer restrictions in daily living.

The purpose of this study is to develop a feedback system that can indicate the loads on handrails applied by the trainees visually. In addition, the developed feedback system is assessed in a walking experiment with able-bodied subjects to ensure whether they can recognize and control the loads by using the system.

Manuscript received October 1, 2012.
Part of this work was supported by the "Funding Program for World-Leading innovation R&D on Science and Technology (FIRST Program)," initiated by the Council for Science and Technology Policy (CSTP).
R. Sabe and Y. Sankai are with Cybernics Laboratory, Systems and Information Engineering, University of Tsukuba, Ibaraki 305-8573,Japan (e-mail:sabe@golem.kz.tsukuba.ac.jp,hayashi@golem.kz.tsukuba.ac.jp, sankai@golem.kz.tsukuba.ac.jp)
T. Hayashi is with Tsukuba R&D Center, CYBERDYNE Inc. D25-1, Gakuen Minami, Tsukuba, Ibaraki, 305-0818, Japan
(e-mail : hayashi@golem.kz.tsukuba.ac.jp)

978-1-4673-1497-8/12/$31.00 ©2012 IEEE

II. Development of a Feedback System

A. System Configuration

Figure 2 shows an overview of the system. The developed feedback system consists of the measurement unit and the display unit. The system has been designed to be attached to a commercially available walker. Two measurement units are respectively attached to the right and left handrails of the walker for measuring the loads on handrails. The display unit is mounted at the center of the walker for showing the loads using a graphical user interface (GUI).

The details of the both units are described in the following subsections.

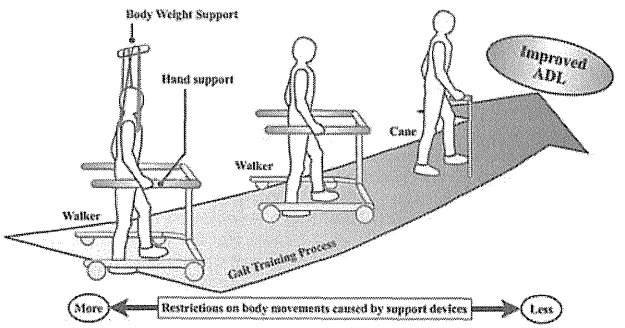

Fig. 1: Gait training process for improving the patients' ADL from the standpoint of the restrictions on body movements caused by support devices.

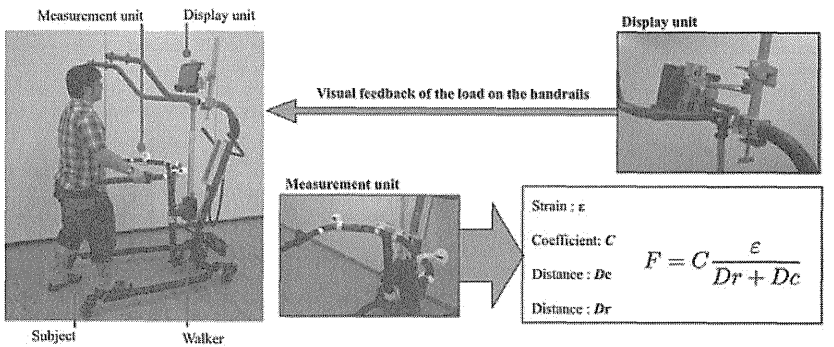

Fig. 2: The developed system for giving the feedback of the loads on handrails to the trainee during gait training. The trainee can know the loads information by looking at the display unit.

B. Measurement unit

The handrail of the walker can be considered as a cantilever beam. On the assumption that the load from the patient is exerted on a point on the handrail, the load on the cantilever beam is shown as

$$F = C\frac{\varepsilon}{D} \qquad (1)$$

where F is the load on the handrail; C is strain coefficient; ε is the strain of the cantilever beam; D is the distance from the load to the point where the strain is measured.

If ε and C are obtained, F can be calculated. In this study, strain gauges and distance sensors were used to obtain them. Figure 3 shows a schematic of the measurement unit. We adopted the two-active gauge method for strain measurement in order to minimize temperature drift. Two strain gauges were attached to the top and bottom surfaces of each the right and left handrail. The developed measurement unit can measure the load caused by a weight suspended from the handrail with an accuracy of ±5 N.

In order to obtain the distance D, the center of the load on the handrail need to be detected. In this study, we assumed that the center of the load is located at the center of the hand grasping the handrail. Dc in Fig. 3 is the distance from the anterior end of the grasping hand to the center of the load. In order to detect the anterior end of the hand, a distance sensor using infrared light was attached at each head of the handrail. To detect the grasping hand clearly, the reflection module was put just ahead of the hand as shown in Fig. 3. The distance measured by the distance sensor is indicated as Dr in Fig. 3.

The measured strain is amplified and filtered by an analog

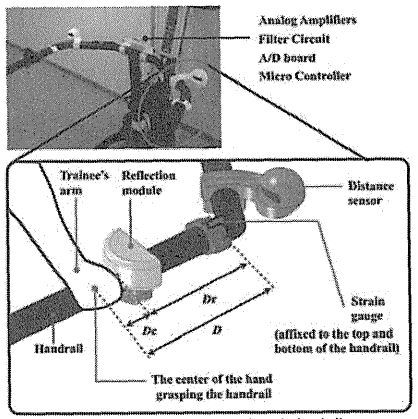

Fig. 3: Schematic of the measurement unit on the handrail.

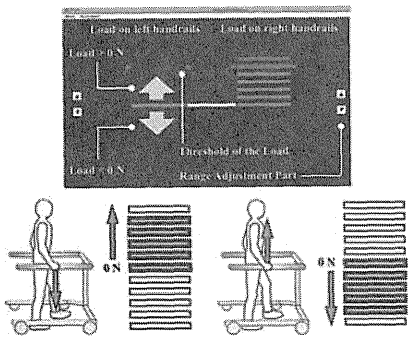

Fig. 4: Graphical User Interface for showing the loads to the trainee while walking. The threshold of the loads and the range for showing loads can be adjusted by using this GUI. The value of the load becomes plus and bar graph extends up when the trainee pushes down the handrails, and the load becomes minus and bar graph extends down when the trainee pulls up the handrails.

preprocessing circuit and converted into digital signals with 100 Hz sampling frequency. The processed signals are transmitted to the display unit via wired Ethernet using the user datagram protocol.

C. Display unit

A tablet PC is used as the display unit. It receives the load signals from the right and left measurement units and shows them on its display.

The tablet PC was mounted on the walker by using a monitor arm. The monitor arm is designed to be able to adjust the height and angle of the display of the tablet PC in accordance with each trainee's height.

Fig. 4 shows the GUI screen for showing the load information on the tablet PC. The green bars displayed at the right and left sides on the screen indicate the loads on the right and left handrails respectively. The displayed loads are updated in real time. One step of the bar corresponds to 10N. The threshold value can be chosen for the right and left handrails and inputted into the GUI by the trainer. When the load exceeds the threshold value, the color of the bar graph is changed to red as shown in Fig. 4. By using the different colors, the display unit helps trainees to recognize whether the load exceeds the threshold or not. The range of the load can also be adjusted on the GUI.

In order to reduce influence of noise, the measured load signals are smoothed through a moving average (MA) filter. The window size of the MA filter is set to 100 ms. The smoothed load signals are shown on the display to trainees during training.

III. Experiments

A. Outline

The experiment with five able-bodied subjects was carried out in order to ensure whether the subjects are able to control the loads on handrails by using the developed feedback system. The subjects were instructed to adjust the loads in accordance with the reference load indicated by the GUI during the experiment. Error rates between the reference load and the measured load were calculated to evaluate the accuracy of the adjustment of the loads on handrails.

To evaluate the feedback system, the experiment consists of the following two trials: a) in which both the loads on handrails and reference loads were shown to the subjects and b) in which only the reference load was shown to the subjects.

B. Reference Load and Evaluation of Error Rates

The reference load was given to the subjects as follows.

$$\begin{aligned} W_d(t) &= 50u(t-3) \qquad 3 \le t \le 8 \\ W_d(t) &= -50u(t-13) \qquad 13 \le t \le 18 \end{aligned} \tag{2}$$

where $Wd(t)$ is the reference load; $u(t)$ is a step input; t is elapse time. Here, the time interval $3 \leqq t \leqq 8$ is described as the plus interval, and the time interval $13 \leqq t \leqq 18$ is described as the minus interval. In order to evaluate the developed feedback system in both cases in which subjects adjust the loads by pushing handrails and by pulling handrails, the reference load was set to +50 N and -50 N.

The error rate was evaluated by root means square error (*RMSE*) as

$$RMSE = \sqrt{\frac{1}{T}\sum_{t=1}^{T}\left[W(t) - W_d(t)\right]^2} \tag{3}$$

where $W(t)$ is the loads on handrails; T is the total time spent on showing each reference load. The reduced *RMSE* means that subjects can adjust the loads appropriately in accordance with the reference load.

C. Protocol

The walking experiment was carried out with 5 able-bodied subjects in their 20s from AS1 to AS5. The range for showing loads was preliminarily selected from -100 N to 100 N. At first, the subjects were instructed to fix the reflection modules on handrails and positioned the tablet PC according to their height. After finishing this procedure, subjects were instructed by the GUI to start walking and to adjust the loads to the reference load indicated by the GUI. Preliminarily, they were instructed not to be conscious of the loads at the block time when $0 \leqq t \leqq 3$, $8 \leqq t \leqq 13$ and $18 \leqq t \leqq 21$. They were also instructed to walk in a straight line at comfortable speed. The trial b) was carried out 10 times for each subject, and after that, the trial a) was also carried out 10 times for each subject. In order to exclude the effect of practice to the system in the trial b), the result of the loads on handrails was not given to the subjects during the walking experiment. The same reference load was used during the 20 times walking experiment in order to remove effects upon the RMSE caused by the difference of the reference load.

IV. Results

Figure 5 shows the representative result of the walking experiment. From the result, we verified that variance of the load data was reduced by giving the load feedback to AS1 at the plus interval. We also verified that the variance was reduced with the developed system at minus interval. The result of RMSE are shown in Table 1 and Fig. 6. From the results, we verified that the average of the *RMSE* was 50 N at plus interval, and 23 N at minus interval in the trial b). We also verified that the average of the *RMSE* was 17 N at plus interval, and 19 N at the minus interval in the trial a). From this we verified that the *RMSE* was reduced when the load information was shown to the subjects by using the developed feedback system during the walking experiment.

A statistical test was performed to verify whether there is a significant difference between the cases in which the feedback was applied to the subjects and in which the feedback was not applied to them. Since the samples are paired, the dependent t-test for paired samples is used as a statistical test. A significance level of the t-test was set to 5%. As a result, the value of t was 5.31 at plus interval and 4.37 at minus interval. Because the value of t is 3.25 when the significance level of the t-test is set to 1 %, we verified that there was a significant difference in the *RMSE* of the load data both at the plus interval and the minus interval.

V. Discussion

The patients with walking difficulties need support devices in their daily lives because they have difficulty of assisting their own body weight. Hence practicing to reduce the loads on handrails during gait training is beneficial for reducing the dependence on support devices and improving their ADL.

In this study, we developed the new feedback system for gait training. The developed system measures the loads on the handrails of the walker and show that load information to trainees by using the tablet PC.

As the result of the walking experiment with five able-bodied subjects, we verified that both the variance and the RMSE of the load data were reduced in the trial a). By applying the dependent t-test for paired samples, we also verified that the average of RMSE was significantly minor when the load information was shown to the subjects. These results clearly indicate the advantage of the developed feedback system for the trainees to control the loads on handrails appropriately during gait training.

In the walking experiment, considering the both cases in which the trainees pull up handrails and the trainees push down handrails in order to support their own body, we chose reference load -50N and 50N. From results, the variance at the minus interval was less than that at the plus interval in the trial b). Additionally, the RMSE produces the same results as the variance' result. These results mean that subjects could adjust the load more appropriately when -50N was indicated as the reference load by the system. The reason is considered to be that people are used to hold something with their hands while walking, but they are unaccustomed to push something by their hands at a certain amount of force while walking in daily living.

Confining the reference load to 50N and -50N in the walking experiment remains a matter of debate, because the pressure feeling differs in subjects. Thus, about the walking experiment, we did not quantitatively investigate the links between the reference load and the RMSE. However, with respect to the feedback system, we confirmed that the system could show the load information to the subjects and they could control the load more appropriately with the developed system.

In this study, the efficacy of the developed feedback system was verified by the walking experiment with able-bodied subjects. In future research, we plan to evaluate the efficacy of the load feedback by carrying out the experiment with the patients who have walking difficulties. It is important for patients to reduce the load in accordance with the reference load during gait training in an effort to reduce the dependence on support devices and switch support devices to the ones with fewer restrictions. Therefore, adjusting the reference load is believed to be linked to the degree of difficulty of gait training. We plan to investigate the way to adjust the value of reference load to the patients' grade of severity in future research.

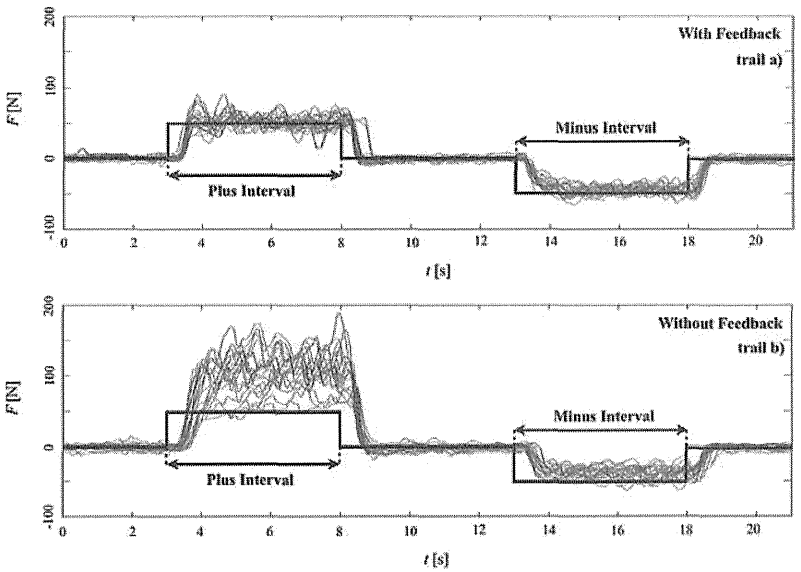

Fig. 5: Result of the walking experiment for AS1 as a representative result. The blue lines show the left load, and the red lines show the right load. The black line indicates the reference load that was set to 50 N at the plus interval and -50 N at the minus interval during the walking experiment. The load data was continuously stored and the error rate was evaluated by RMSE. The RMSE at the plus interval was calculated between t=3 and t=8, and the RMSE at the minus interval was calculated between t=13 and t=18.

Table 1: Result of the RMSE of the loads at the plus interval and the minus interval

Plus Interval

AS ID	Left / Right	RMSE [N] without Feedback	RMSE [N] with Feedback
1		56	17
		55	18
2		43	16
		39	17
3		53	19
		47	17
4		26	17
		25	20
5		87	16
		66	18
Average		50	17
Standard deviation		17.7	1.2

Minus Interval

AS ID	Left / Right	RMSE [N] without Feedback	RMSE [N] with Feedback
1		21	17
		21	18
2		25	22
		23	21
3		26	17
		20	18
4		26	21
		22	19
5		22	21
		22	21
Average		23	19
Standard deviation		2.2	1.7

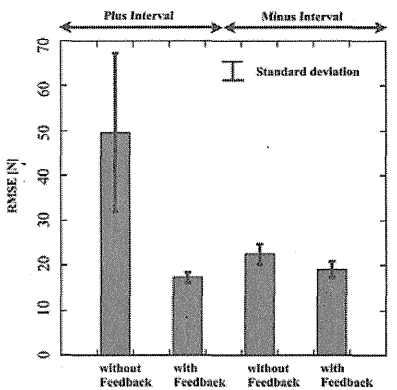

Fig. 6: Result of the RMSE during walking experiment. The bar graphs indicate the average of the RMSE in each case.

VI. Conclusion

In this research, we developed a new feedback system for showing how much load a trainee is applying on handrails during gait training. The developed system was ensured in the walking experiment. The system effectively gives feedback of the load information to the able-bodied subjects and assists them to adjust the load appropriately in accordance with the reference load indicated by the system. This feedback system would help the patients with walking difficulties to improve their gait and improve their ADL.

References

[1] Y. Baram, R. Lenger, "Gait improvement in patießnts with cerebral palsy by visual and auditory feedback," *Virtual Rehabilitation International Conference*, pp.146-149, 2009.

[2] E. Isakov, "Gait rehabilitation: a new biofeedback device for monitoring and enhancing weight-bearing over the affected lower limb," *European Journal of Physical and Rehabilitation Medicine*, Vol. 43, No. 1,pp. 21-26, 2006.

[3] B. Joonbum, K,, Kyouguchi, K., B., Nancy, T., Masayoshi, "A Mobile Gait Monitoring System for Abnormal Gait and Rehabilitation : A Pilot Study for Parkinson Disease Patients." *Journal of Biomechanical Engineering*, Vol. 133, No. 4, pp. 1-11, 2011

[4] J.M. Stacy, A.P. Joseph, "SHOE-INTEGRATED SENSOR SYSTEM FOR WIRELESS GAIT ANALYSIS AND REAL-TIME FEEDBACK", *Biomedical Engineering Society*, Vol. 3, pp. 2468-2469, 2002

[5] A. Ledebt, J. Becher, J. Kapper, R.M. Rozendaalr, R. Bakker, I.C. Leenders, G.J. Savelsbergh, "Balance training with visual feedback in children with hemiplegic cerebral palsy: effect on stance and gait", *Motor Control*, Vol. 9, No. 4, pp. 459-468, 2005

[6] D. Erbil, D. Nigar, A. Duygu, "Effects of biofeedback treatment on gait in children with cerebral palsy", *Disability and rehabilitation*, Vol. 26, No. 2, pp. 116-120, 2004

[7] S. Abhishek, B.T. Arun, G. Anupam, K. Senthil, M. Thyloth, "Post-stroke balance training: Role of force platform with visual feedback technique", *Journal of the Nwurological Science*, Vol. 287, No. 1-2, pp. 89-93, 2009

[8] E. Aiello, D.H. Gates, B.L. Patritti, K.D. Cairns, M. Meister, E.A. Clancy, and P. Bonato,"Visual EMG Biofeedback to Improve Ankle Function in Hemiparetic Gait", *Engineering in Medicine and Biology Society*, pp. 7703-7706, 2005

2012 IEEE/SICE International Symposium on System Integration (SII)
Kyushu University, Fukuoka, Japan
December 16-18, 2012

Noise-Resistant Vascular Parameter Identification for Artery Testing

Hayato Koba, Kinichi Nakata, and Yoshiyuki Sankai

***Abstract*—Artery testing prevents us from atherosclerotic disease and several methods to evaluate physiological change are performed. However, comprehensive estimation methods of physiological characteristics of blood vessel are not well established and measured data are influenced by physiological conditions. Vascular system model can improve artery testing because parameters of the model indicate the characteristics of blood vessel. Our laboratory has been developing vascular system model and identification method of the model, which can estimate the characteristics of blood vessel. The purpose of this study is to construct and verify a noise-resistant method of vascular parameter identification for artery testing that can identify the parameter accurately regardless of noise. We developed a physiological model of vascular system and parameter identification method. The identification method includes filter that can eliminate noise. In order to verify the performance of the identification method, we carried out a computer simulation experiments. We constructed a physiological model on a computer with preset parameters. Simulations were performed in several different parameter settings with data that contain 10% white noise. We also performed simulations using data with 5% and 20 % white noise. Identification results showed that maximum values of errors were 0.7200%, 4.947% and 11.56% for data with 5%, 10% and 20% noise intensity, respectively. Those results showed that our method was able to reduce influence of noise and to identify the vascular parameters accurately regardless of noise.**

I. Introduction

OUR motivation to develop a new method for artery testing is to save human lives from diseases originated in atherosclerosis whose mortality is more than 13 million in the world [1]. Arteries of patients who suffer from atherosclerosis harden and narrow due to lumped fat. Then narrowing will obstruct blood flow. Doctors recommend patients to have artery testing in order to prevent atherosclerotic disease by motivating patients to healthful lifestyle and detecting early physiological changes [2]. Physiological characteristics of blood vessels, such as narrowing and hardening, are important in artery testing. Several methods to evaluate the characteristics of blood vessel are performed.

Manuscript received October 1, 2012. Part of this work was supported by the "Funding Program for World-Leading Innovative R&D on Science and Technology (FIRST Program)," initiated by the Council for Science and Technology Policy (CSTP).

Hayato Koba and Yoshiyuki Sankai are with Cybernics Laboratory, Systems and Information Engineering, University of Tsukuba, Ibaraki 3058006 Japan (phone and fax: +81-29-853-2883; e-mail: koba@golem.kz.tsukuba.ac.jp; sankai@golem.kz.tsukuba.ac.jp).

Kinichi Nakata is with Department of Cardiovascular Surgery, Nihon University School of Medicine, Itabashi, Tokyo 1738610 Japan (e-mail: poohnakata@aol.com).

Measuring blood flow using ultrasound is widely performed for blood vessel testing [3]. In severely narrowed artery, reduction of blood flow occurs due to high blood flow resistance. Blood flow resistance is defined as ratio of blood pressure to blood flow volume [4]. Even if low blood flow is observed during artery testing, it is difficult to distinguish whether the flow reduction comes from narrowed artery or peripheral blood vessels.

Pulse wave velocity (PWV) is also widely performed for artery testing [5]. Higher PWV value indicates hardening of arteries because transit speed of pulse wave of blood pressure in hardened artery is faster than healthy artery. However PWV is influenced not only by hardening but also by blood pressure, narrowing artery and several factors related to health problem.

Current clinical scene does not know a method to comprehensively estimate physiological characteristics of blood vessel and physiological state. The characteristics of blood vessel are described in mathematical model of vascular system [6]-[8]. Artery testing will improve if parameters of the vascular system model (vascular parameter) are employed for artery testing because vascular parameters indicate the characteristics of blood vessel. However, artery testing using vascular system models is hardly performed in clinical use because of complexity of the model and difficulty to identify vascular parameters. The reason of difficulty of vascular parameter identification is that the characteristics of vascular system are internal physiological data of living body and are not measured directly.

In order to solve those problems, our laboratory has been developing simple but enough detailed vascular system model and identification method of vascular parameters [9]-[13]. This identification method enables us to identify vascular parameters by measuring continuous waveforms of blood pressure and blood flow volume. When vascular parameters are identified for artery testing, noninvasive measurement of continuous waveforms of blood pressure and blood flow volume is needed. However, identification result will be disturbed if measurement data contains noise. Possibility that noninvasive method contains noise is large compared to invasive method. In order to improve artery testing, the purpose of this study is to construct and verify a noise-resistant method of vascular parameter identification for artery testing that can identify the vascular parameter accurately regardless of noise. We verified the identification method through computer simulation experiments.

978-1-4673-1497-8/12/$31.00 ©2012 IEEE

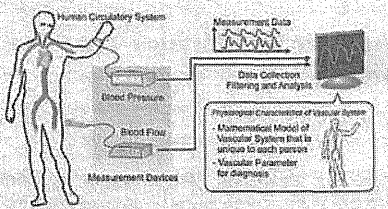

Fig. 1. Vascular Parameter Identification for artery testing requires integration of measurement information and rapprochement between living body and physiological model on computer.

II. Vascular Parameter Identification

Figure 1 shows the schematic of vascular parameter identification. Continuous waveforms of blood pressure and blood flow volume are measured and collected into computer. Computer with algorithm of vascular parameter identification performs filtering and calculation. Integration of measurement data and rapprochement between living body and physiological model are important for vascular parameter identification for artery testing.

A. Vascular System Model

We have constructed a physiological model for vascular system in previous research [9]-[13]. Using fluid dynamics theory and physiological knowledge, we obtained a model described in relationship of blood pressure to blood flow volume as shown in fig 2.

We applied Navier-Stokes equation to describe the flow motion of blood in blood vessel because blood is an incompressible fluid. In terms of viscosity, we assumed the blood flow belongs to Poiseuille theory. In terms of inertia, we extracted dominant terms. We also considered pressure-volume relationship of inside of blood vessel. By applying those theories, the characteristics of blood vessel are described as physiological parameters and a blood vessel model is obtained. In order to obtain vascular system model, we sequentially connected the blood vessel model of artery, peripheral circulation and vein by treating vascular system as a lumped element circuit. By assuming complex vascular system as a linear system and extracting dominant parameters, we constructed a vascular system model. The constructed model is represented as below:

$$\begin{cases} \dfrac{d}{dt}\begin{bmatrix} x_1 \\ x_2 \end{bmatrix} = \begin{bmatrix} -\dfrac{L+R_aR_pC}{R_pCL} & 1 \\ -\dfrac{R_a+R_p}{R_pCL} & 0 \end{bmatrix}\begin{bmatrix} x_1 \\ x_2 \end{bmatrix} + \begin{bmatrix} \dfrac{1}{L} \\ \dfrac{1}{R_pCL} \end{bmatrix} P(t) \\ Q(t) = \begin{bmatrix} 1 & 0 \end{bmatrix}\begin{bmatrix} x_1 \\ x_2 \end{bmatrix} \end{cases} \quad (1)$$

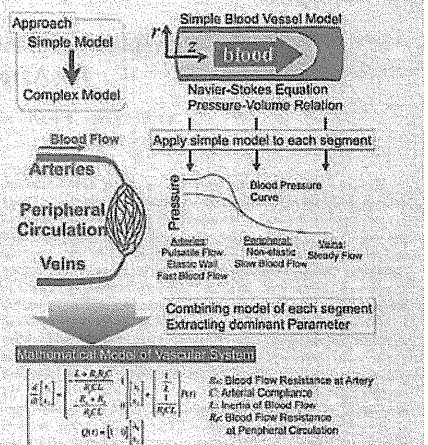

Fig. 2. Modeling vascular system was based on fluid dynamics theory and physiological knowledge. We obtained vascular system model by combining simple model of blood vessel and extracting dominant parameters.

t is time. $P(t)$ [mmHg] and $Q(t)$ [ml/min] are measured arterial blood pressure and blood flow volume. $x_1(t)$ and $x_2(t)$ are state variables. L [mmHg min min/ml], R_a [mmHg min/ml], C [ml/mmHg] and R_p [mmHg min/ml] correspond to inertia of blood flow, blood flow resistance at artery, compliance at artery, and blood flow resistance at peripheral circulation, respectively.

Figure 3 shows a relationship between physiological characteristics of blood vessel and important vascular parameters for artery testing. R_a and C are important parameters for artery testing because those parameters are related to narrowing and hardening of blood vessel that are physiological change of atherosclerosis. When tested artery is narrowed, value of R_a is higher than R_a of healthy artery. When tested artery is hardened, value of C is lower than C of healthy artery. Those parameters tell us physiological characteristics of blood vessel, which is estimated comprehensively.

B. Noise-Resistant Method of Parameter Identification

Figure 4 shows a schematic of parameter identification algorithm for vascular parameter. Parameters of the model are identified from continuous waveforms of measured blood pressure and blood flow volume by using recursive least square method [9]-[13]. We employed this method for vascular parameter identification method for artery testing. The identification algorithm using delta operator with noise filter is represented as below:

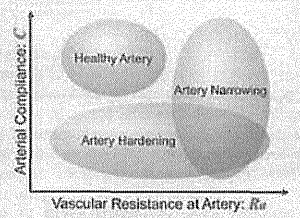

Fig. 3. R_a and C are important for artery testing. When tested artery is narrowed, value of R_a is higher than R_a of healthy artery. When tested artery is hardened, value of C is higher than C of healthy artery.

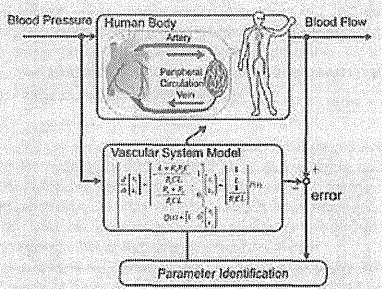

Fig. 4. Parameter identification algorithm consists of actual blood circulation of human body, vascular system model, parameter identification and data from human body.

$$\delta\theta_k = \frac{1}{T_s}\frac{D_{k-1}\varphi_k}{1+\varphi_k' D_{k-1}\varphi_k}\left[Q_k - \varphi_k'\theta_k\right] \tag{2}$$

$$\delta D_{k-1} = -\frac{1}{T_s}\frac{D_{k-1}\varphi_k\varphi_k' D_{k-1}}{1+\varphi_k' D_{k-1}\varphi_k} \tag{3}$$

where

$$\varphi_k = \left[\frac{\delta Q_k}{E(\delta)} \quad \frac{Q_k}{E(\delta)} \quad \frac{\delta P_k}{E(\delta)} \quad \frac{P_k}{E(\delta)}\right]^t \tag{4}$$

$$\theta_k = \left[e_1 - \frac{L+R_aR_pC}{R_pCL} \quad e_0 - \frac{R_a+R_p}{R_pCL} \quad \frac{2R_pCL - R_aR_pCT_s}{2R_pCL^2} \quad \frac{2L - R_aT_s - R_pT_s}{2R_pCL^2}\right]^t \tag{5}$$

$$\frac{1}{E(\delta)} = \frac{1}{\delta^2 + e_1\delta + e_0} \tag{6}$$

$$\delta Q_k = \frac{Q_{k+1} - Q_k}{T_s}, \tag{7}$$

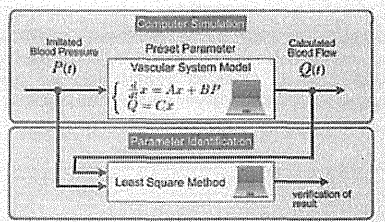

Fig. 5. Computer simulation experiments consist of computer simulation and parameter identification. Vascular system model with preset parameters is constructed in a computer. Calculated blood pressure that imitates actual blood pressure was input to the model and blood flow was simulated. Noise was added to both blood pressure and blood flow.

δ is the operator for describing the discrete time model. A stable filter $E(\delta)$ is called state variable filter, which eliminates noise. Both e_1 and e_2 are the coefficient of the filter. T_s is the sampling period. k is sample numbers.

This algorithm identifies vascular parameters and estimates physiological characteristics of blood vessel quantitatively using blood pressure and blood flow that are non-invasively during artery testing. Although measurement equipment implements filter, possibility that data contains noise still remains because of noise such as electromagnetic noise on circuits and those on cables. This algorithm is resistant to noise because the algorithm is integrated with a stable filter. From those points, two filters, filter in measurement equipment and filter in identification algorithm, are used in this method. Those duplex filters provide robustness with respect to noise for vascular parameter identification for noninvasive artery testing. Identified vascular parameters are put to good use for artery testing because those parameters indicate the characteristics of blood vessel.

III. Computer Simulation Experiments

Figure 5 shows schematic of computer simulation experiments. In order to verify the performance of the identification method, we carried out computer simulation experiments. Physiological models with preset parameters were constructed on a computer. We input imitated blood pressure data to the model in order to simulate blood flow volume. Simulation was performed by Euler method at simulation step of 5 [ms]. Both blood pressure and blood flow were added white noise separately. We performed parameter identification using imitated blood pressure and simulated blood flow to evaluate the performance of the identification method. We verified the identification method in two experiments, experiment A and B. In experiment A, we employed different parameter settings for computer simulation. Identification was performed using data with noise of 10% intensity. In experiment B, we employed different settings of noise intensity for computer simulation and parameter identification. Noise intensity is expressed as percentage to amplitude of each waveform. We evaluate the performance of the identification method by calculating error between preset parameters and identified parameters.

TABLE I
PRESET VASCULAR PARAMETERS FOR EXPERIMENT A

	R_a	C	L	R_p
Default	0.3000	0.1000	0.03000	1.200
High R_a	0.6000	0.1000	0.03000	1.200
Low C	0.3000	0.08000	0.03000	1.200
High R_p	0.3000	0.1000	0.03000	2.000

In computer simulation experiment, vascular system model with preset parameter was constructed in computer. Several parameter sets were prepared to verify the performance of our method.

TABLE 2
PRESET VASCULAR PARAMETERS FOR EXPERIMENT B

	R_a	C	L	R_p	*Noise Intensity*
Default	0.3000	0.1000	0.03000	1.200	10
Low Noise	0.3000	0.1000	0.03000	1.200	5
High Noise	0.3000	0.1000	0.03000	1.200	20

Different noise intensity was set in order to verify the performance of our method. Noise intensity is expressed as percentage to amplitude of each waveform.

A. Different Parameter Settings with 10% Noise

In order to verify that our method can identify the vascular parameter accurately in different characteristics of blood vessel, several parameter settings were prepared as shown in table 1. We prepare parameter set of high R_a that indicates artery narrowing. We prepare parameter set of low C that indicates artery hardening. We prepare parameter set of high R_p that indicates change of physiological state. Simulations and identification of each parameter set were performed individually.

B. Different Noise Intensity Settings

In order to verify that our method can identify the vascular parameter accurately in different noise intensity, we performed simulations with different noise intensity. Table 2 shows parameters and noise intensity settings in experiment B. Noise intensity settings were 10% as default condition, 5% as low noise intensity condition and 20% noise as high noise intensity condition. Simulation with 10% noise is same as simulation of default parameter setting in experiment A. Simulations and identification of each parameter set were performed individually.

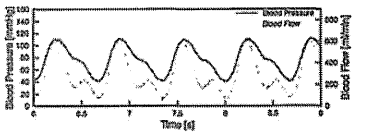

Fig. 6. The result of computer simulation with default parameter setting and noise intensity is shown. Blood flow was simulated from imitated blood pressure.

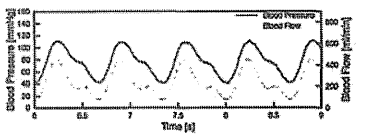

Fig. 7. The result of computer simulation with of high R_a is shown. Maximum blood flow volume was lower than the result of simulation with default parameter setting.

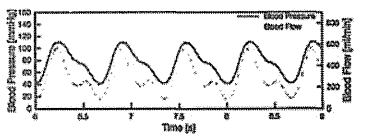

Fig. 8. The result of computer simulation with parameter set of low C is shown. Amplitude of blood flow waveform was reduced compared to the result of simulation with default parameter setting.

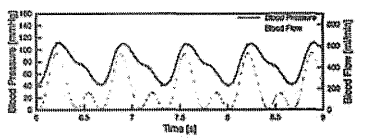

Fig. 9. The result of computer simulation with parameter set of high R_p is shown. Blood flow volume was lower than the result of simulation with default parameter setting. Minimum blood flow was lower than the simulation with parameter set of high R_a.

IV. Results

A. Different Parameter Settings with 10% Noise

Figure 6 to figure 9 show results of computer simulations in experiment A. In all figures, black line shows blood pressure and gray line shows blood flow volume. Through the computer simulation experiment, blood flow was simulated.

TABLE 3
IDENTIFIED PARAMETERS IN EXPERIMENT A

	R_a	C	L	R_p
Default	0.3057	0.1010	0.03004	1.195
High R_a	0.5973	0.09982	0.03105	1.204
Low C	0.3148	0.08238	0.02985	1.186
High R_p	0.3037	0.1005	0.02992	1.996

All vascular parameters were identified in all parameter settings in the experiment A from simulated data with

TABLE 4
ERROR OF IDENTIFIED PARAMETERS IN EXPERIMENT A

	R_a	C	L	R_p
Default	1.913	0.9760	0.1433	0.4000
High R_a	0.4517	0.1810	3.490	0.3250
Low C	4.947	2.976	0.4933	1.183
High R_p	1.220	0.4770	0.2600	0.2050

Error values between preset parameters and identified parameters in experiment A were calculated. Error is expressed as percentage to true value of parameter. Maximum error was 4.947%, which is error of R_a in result simulation with low C.

Figure 7 shows reduction of maximum blood flow compared to default parameter setting. Figure 8 shows reduction of amplitude of blood flow volume compared to default parameter setting. Figure 9 shows total blood flow reduction compared with default parameter setting.

All vascular parameters were identified using those simulation data. Table 3 shows identified parameters. Error values between preset vascular parameters and identified vascular parameters are shown in table 4. Maximum error was 4.947%, which is error of R_a in result of simulation with low C setting.

B. Different Noise Intensity Settings

Figure 10 shows the result of the computer simulation with 5% noise intensity. Figure 11 shows the result of the computer simulation with 20% noise intensity condition. In both figures, black line shows blood pressure and gray line shows blood flow volume. Through the computer simulation experiment, blood flow was simulated.

Figure 10 shows decrease of noise compared to the simulation result of default noise intensity that is shown in fig. 6. Figure 11 shows increase of noise compared to the simulation result of default noise intensity.

All vascular parameters were identified using those simulation data with different noise settings. Table 5 shows identified parameters. Error values between preset vascular parameters and identified vascular parameters are shown in table 6. In experiment B, maximum error was 0.7200%, 1.913% and 11.56% for data with 5%, 10% and 20% noise intensity, respectively.

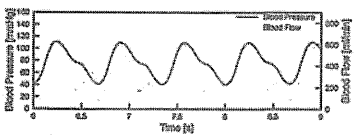

Fig. 10. The result of computer simulation with 5% noise is shown. Less noise was observed compared to the result of simulation with default setting.

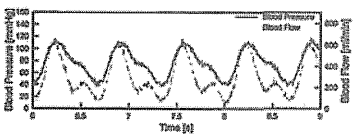

Fig. 11. The result of computer simulation with 20% noise is shown. Larger noise was observed compared to the result of simulation with default setting.

TABLE 5
IDENTIFIED PARAMETERS IN EXPERIMENT B

	R_a	C	L	R_p
Default	0.3057	0.1010	0.03004	1.195
Low Noise	0.3014	0.1004	0.03022	1.199
High Noise	0.3347	0.1048	0.02924	1.165

All vascular parameters were identified from data contains noise of each noise intensity setting in the experiment B. Result of default noise intensity is same as result of default parameter setting in experiment A.

TABLE 6
ERROR OF IDENTIFIED PARAMETERS IN EXPERIMENT B

	R_a	C	L	R_p
Default	1.913	0.9760	0.1433	0.4000
Low Noise	0.4667	0.4280	0.7200	0.05833
High Noise	11.56	4.764	2.530	2.900

Error values between preset parameters and identified parameters in experiment B were calculated. Error is expressed as percentage to true value of parameter.

V. DISCUSSION

In order to improve artery testing, vascular system model is useful for comprehensive evaluation for physiological characteristics of blood vessel because vascular parameter indicates the characteristics of blood vessel. Our laboratory has been developing the mathematical model of vascular system and identification method for vascular parameters. In this study, we constructed and verified a method for vascular parameter identification for artery testing that includes filter in identification algorithm. We carried out experiments in order to verify the performance of the identification method to identify the vascular parameter accurately.

Through the computer simulation experiments, blood flow was simulated in all parameter setting and noise intensity. All vascular parameters were identified using imitated blood pressure and simulated blood flow volume.

In experiment A, simulated blood flow varied with different parameter settings. Simulation result with high R_a showed reduction of maximum blood flow compared to default parameter setting due to high blood flow resistance. Simulation result with low C showed reduction of amplitude of blood flow volume compared to default parameter setting due to less elasticity of blood vessel. Simulation result with low R_p showed total blood flow reduction compared with default parameter setting due to high blood flow resistance at peripheral circulation. In experiment A, the maximum error of the parameter was 4.947%, which is smaller error compared to noise intensity of 10%.

In experiment B, waveform of blood pressure and blood flow contains noise. Simulation results reflect differences of noise intensity settings. Values of maximum error in experiment B were 0.7200%, 1.913% and 11.56% for data with 5%, 10% and 20% noise, respectively. All error was smaller than noise intensity that means error between actual waveform and measured waveform.

Those result shows that error values of identified parameters were less than noise that means error of measured data. We confirmed that we were able to construct a method of vascular parameter identification for artery testing that can identify the vascular parameter accurately regardless of noise. In order to establish a new clinical index with vascular parameter identification for artery testing, studies of measurement on living body to verify the noise-resistant vascular parameter identification method are needed. Vascular parameters will be identified in more amounts of subjects including subjects who have a sign of atherosclerotic disease in order to establish the standard of vascular parameter values.

VI. CONCLUSION

In order to identify the vascular parameter accurately regardless of noise, we constructed a method of vascular parameter identification for artery testing that include filter in the identification algorithm. We verified the identification method through computer simulation experiments. Results of experiments showed that error of identified parameters was less than noise intensity that means error between actual data and measured data. We demonstrated that we were able to construct a noise-resistant method of vascular parameter identification for artery testing that can identify the vascular parameters accurately regardless of noise.

Vascular parameter indicates physiological characteristics of blood vessel, which is important information for artery testing. In order to improve artery testing by employing vascular parameter, the values of vascular parameter should be standardized. We hope our study will contribute to improvement of artery testing and to reduction of the mortality of atherosclerotic disease.

REFERENCES

[1] S. Mendis, P. Puska and B. Norrving, *Global Atlas on cardiovascular disease prevention and control*. Geneva: The World Health Organization in collaboration with the World Heart Federation and the World Stroke Organization, 2011, ch. 1.

[2] S. L. Yesenko, S. M. Whitelaw, and H. L. Gornik, "Testing in the Noninvasive Vascular Laboratory," *Circulation*, vol. 115, pp. e624-e626, June 2007.

[3] M. Gerhard-Herman, J. M. Gardin, M. Jaff, E. Mohler, M. Roman, and T. Z. Naqvi, "Guidelines for noninvasive vascular laboratory testing: a report from the American Society of Echocardiography and the Society for Vascular Medicine and Biology," *Vasc. Med*, vol. 11, pp. 183-200, Nov. 2006.

[4] J. R. Levick, *An Introduction To Cardiovascular Physiology*. London: Hodder Arnold, 2010, pp. 6-15.

[5] J. M. Padilla, E. J. Berjano, J. Saiz, L. Facila, P. Diaz, S. Merce, "Assessment of relationships between blood pressure, pulse wave velocity and digital volume pulse," *Computers in Cardiology*, pp. 893-896, 2006.

[6] M. G. Taylor, "Use of random excitation and spectral analysis in the study of frequency dependent parameters of the cardiovascular system," *Circ. Res.* Vol. 18, pp. 585-595, 1966.

[7] Y. C. Yu, J. R. Boston, M. A. Simaan, J. F. Antaki, "Estimation of systemic vascular bed parameters for artificial heart control," *IEEE Trans. Automatic Control*, vol. 43, no. 6, pp. 765-778, Jun 1998.

[8] M. J. Conlon, D. L. Russell, T Mussivand, "Development of a mathematical model of the human circulatory system," *Ann. Biomed. Eng.*, vol. 34, pp. 1400-1413, Sept. 2006.

[9] R. Kosaka, Y. Sankai, T. Jikuya, T. Yamane, T. Tsutsui, "Online Parameter Identification of Second-Order Systemic Circulation Model Using the Delta Operator," *Artif. Org.*, vol. 26, no.11, pp. 967-970, Nov. 2002.

[10] R. Kosaka, Y. Sankai, T. Yamane, and T. Tsutsui, "Estimation of a physiologic strategy based on a mathematical model for assisting and substituting cardiac functions by a robotic artificial heart," *ADVANCED ROBOTICS*, Vol. 19, pp.735-749, Aug. 2005.

[11] R. Kosaka, Y. Sankai, T. Yamane, T Tsutsui, "Resonant Frequency Control Method for Total Artificial Heart: in Vitro Study," *Artif. Org.*, vol. 32, no. 2, pp. 157-160, Feb. 2007.

[12] R. Kosaka, Y. Sankai, T. Jikuya, T. Yamane, and T. Tsutsui, "Online Parameter Identification of Systemic Circulation Model Using Delta-Operator in Animal Experiment," in *Proc. of IEEE/RSJ IROS 2002*, Lausanne, 2002 , pp. 1469-1474.

[13] H. Koba, K. Nakata, K. Akiyama, Y. Orime, T. Takamori and Y. Sankai, "Assessment of Vascular Resistance at Artery by using Mathematical Model of the Vascular System: Verification by Animal Experiments," *Trans. Jap. Soc. Med. and Biolog. Eng.*, vol. 49, no. 1, pp. 84-90, 2011. (in Japanese)

Wearable Parallel Processing Based High-Resolution High-Speed Electroencephalogram Monitoring Integrated System

Alexsandr I. Ianov, Hiroaki Kawamoto and Yoshiyuki Sankai

Abstract — **Daily use of electroencephalogram (EEG) could increase the effectiveness for medical applications. However, current brain monitoring technologies lack one or more characteristics necessary for daily use, such as portability, responsiveness or versatility. In this study we developed a portable prototype for high resolution real-time EEG monitoring fully integrated system. The prototype is composed of 112 custom made hybrid capacitive-resistive electrodes and up to 7 reference electrodes. The electrodes are connected together by using a flexible, elastic grid which is attached to an adjustable, link based mechanical headgear. Real time processing was performed using a mobile Compute Unified Device Architecture (CUDA) platform for massive parallel processing of the data. Experiments to test the capabilities of the prototype were performed. The first experiment consisted of monitoring the frontal lobe when applying visual stimulus using a lamp. When the lamp was turned on weak alpha waves were detected, while when the lamp was turned off alpha waves were detected. The second experiment consisted of monitoring the entire motor cortex while moving the right hand. At rest, strong mu-rhythm signals were detected over the entire scalp above the motor cortex whereas when moving the right hand mu-rhythm signals above the left motor cortex area were weakened. Both experiment results matched known brain activity phenomena demonstrating basic monitoring capabilities of the prototype. Furthermore we showed that our system has high portability, usability and capable of high responsiveness on high resolution conditions. The concepts introduced in this paper can not only improve EEG monitoring technologies but also contribute to other areas of wearable computing.**

I. Introduction

BRAIN activity monitoring technologies are fundamental tools in the treatment of neurological disorders, rehabilitation techniques, assistive device interfacing methods[1]-[3] and are becomes increasingly important in social and entertainment aspects of wearable computing. Depending on the patient or situation, constant monitoring during daily life is desirable or required. Electroencephalography (EEG) monitoring has been traditionally suggested for daily brain activity monitoring as compared to Magnetic Resonance Imaging (MRI) or Magnetoencephalography (MEG) it is a much cheaper, smaller and versatile solution.

Manuscript received September 18, 2012. Part of this work was supported by the "Funding Program for World-Leading Innovative R&D on Science and Technology (FIRST Program)," which was initiated by the Council for Science and Technology Policy (CSTP).

All the authors are with Cybernics Laboratory, System and Information Engineering, University of Tsukuba, Ibaraki 305-8573, Japan (e-mail: ianov@golem.kz.tsukuba.ac.jp; kawamoto@golem.tsukuba.ac.jp; sankai@golem.tsukuba.ac.jp).

Several EEG technologies are available commercially[4]. Systems such as the BCI2000[5] and the G.Tec (Guger Technologies, Austria) are widely used in medical and academic facilities. Such systems are capable of high spatial and temporal resolution. However these products rely on passive resistive electrodes requiring the user to perform skin preparation and lose signal quality with time[6]. Moreover such devices are used as nonwearable computer peripherals, as the headgear and electrodes are connected through a series of cables to a standalone Analog-Digital Converters (ADC) unit which is connected to a host personal computer (PC). This design limits the motion freedom of the user and application scope of the system due to the low portability and usability.

By contrast, systems such as the Epoc headset (Emotiv Systems, Australia) or the Mindwave headset (Neurosky Inc., USA) have been developed targeting entertainment applications. These systems are characterized by having high portability and wearability. However, due to the fixed mechanical design they lack the versatility required for several medical and academic applications. Moreover, the limited onboard processing power limits maximum number of channels a headset can have and an external PC is still required for several applications. Furthermore the lag originated from the wireless connection between the PC and the headset is an issue when real-time processing is required.

From an end-user point of view, brain activity monitoring requires a device with high usability and portability that minimizes the impact on daily life of the end-user. From a professional point of view, a device should provide high spatial and temporal resolution for high responsiveness and signal reliability, it should be strong against noise sources and it also should be flexible enough to provide the opportunity for a wide range of applications over the same platform. A common device that can be used by both professionals and end-users would streamline application development as well as increase data consistence. However such device would also require high usability, portability from the end-user requirements as well as the high versatility and reliability from the professional requirements. In previous researches the authors have developed a hybrid capacitive-resistive electrode for bioelectrical signal capable of signal quality comparable with commercial electrodes achieving high reliability while also achieving high usability as no skin preparation is required and the signal does not degrade with time[7][8]. Furthermore, while mobile Central Processing Units (CPUs) are not fast enough to perform data collection and frequency analysis simultaneously and in real time of a large number of sensors at high sampling frequencies, the parallel nature of EEG monitoring is compatible with the concepts of parallel processing using Graphic Processing Units(GPUs). Other researchers have already demonstrated the signal processing capabilities and significant performance advantages of GPUs using Compute Unified Device Architecture (CUDA)[9][10]. By integrating our hybrid electrodes with a mobile, onboard GPU based data processing system using a modular design, a novel wearable all in one EEG monitoring device that provides simultaneously high usability, portability, versatility and reliability can be achieved.

In this study we develop a novel integrated EEG monitoring system combining capacitive bioelectrical measurement and parallel computing technologies. A portable high-resolution EEG monitoring headgear composed of up to 112 sensing electrodes and up to 7 reference custom hybrid capacitive-resistive electrodes was developed. In order to record and analyze the massive amount of data from the headgear, a CUDA based wearable processing system was developed providing real-time signal analysis for each sample at 1 kHz sampling rates.

II. Materials and Methods

A. Hardware Development

In this study hybrid resistive-capacitive electrodes that we previously developed were used as EEG sensors[7][8]. EEG recordings are performed throughout active resistive contact with when the electrodes are capable of electromechanical contact(resistive mode). However, in the case of poor contact conditions, the electrodes capacitive couple with the scalp in order to perform the readings(capacitive mode). Fig.1 shows the equivalent circuit when the electrodes are in use. This model also includes noise from capacitive sources as

$$V_{IN} = \frac{R_e}{Z_{ne}} V_{ne} + \frac{R_e}{Z_{nsei}} V_{nsei} + \frac{R_e}{Z_{sei}} V_{BES} \quad (1)$$

where V_{bes} is the bioelectrical signal voltage, V_{in} is the electrode input voltage, V_{nsei} is the total noise source voltage at the skin-electrode surface, V_{ne} is the total noise source voltage on the electrode board, Z_{sei} is the skin-electrode interface impedance, R_e is the electrode input impedance, Z_{nsei} is the noise input impedance at the skin-electrode interface, and Z_{ne} is the noise input impedance on the electrode board. This noise can be significant if the electrodes are in capacitive mode. However it can be minimized when the sensor input impedance is optimal, when it is large enough to make the sensor electrode to capacitive EEG signals but low enough to reject capacitive noise signals from the environment. Input impedance is optimized using

$$R_e = \frac{V_{IN}}{V_{BES}} \cdot \frac{d}{\varepsilon_r \varepsilon_0 A 2\pi f} \quad (2)$$

where ε_0 is the dielectric constant in vacuum, ε_r is the relative dielectric constant to the material, A is the electrode lead sensing area nearest to the skin, f is the frequency of the target signal and d is the distance between the skin and the electrode lead.Based on this model and assuming a maximum 1 mm distance between the electrode and the scalp, an electrode measuring 14 mm^2, with total sensing area of 8 mm^2, and input impedance of 1 TΩ was developed. Noise frequency spectrum measurement experiments were performed for both resistive and capacitive modes by placing two electrodes face to face on differential input. The results are shown in Fig. 6, Chapter 3.

119 hybrid electrodes were used to assemble a headset, as shown in Fig. 2 and Fig. 3. The headset is composed of two main elements. The first element is a variable link mechanism designed using statistical head anatomical data provided by the Japanese National Institute of Advanced Industrial Science and Technology (AIST)[11]. The flexibility provided by using an articulated link mechanism allows the headset to fit on wide range of head geometries. The second element is an elastic net which is attached to the link mechanism. The elastic net is responsible for keeping the link mechanism closed when worn due to the elastic force towards the inside to the headset as well as being the docking place for the electrodes.

The electrodes are placed as shown in Fig. 4. This placement method is fully compatible with the International 10-20 Method for EEG electrode placement. The electrodes are divided in 7 groups of 16 measurement channels and 1 reference for a total of 112 channels and 7 references. The option for having using only one reference electrode for all measurement channels is also available. Each electrode group is connected to a differential input capable 16 channel 16 bit ADC module as shown in Fig. 5. All electrodes and modules can be freely added or removed based on the user's need. All modules are connected through USB 3.0 to a dual core Intel Atom Based mother-board with a CUDA capable Nvidia Ion 2 chipset.

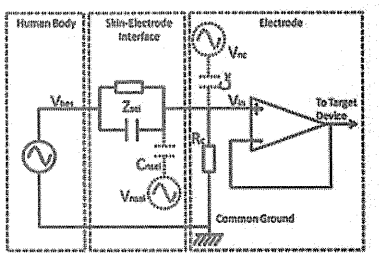

Fig. 1. Electrode equivalent circuit

Fig. 2. EEG monitoring integrated system

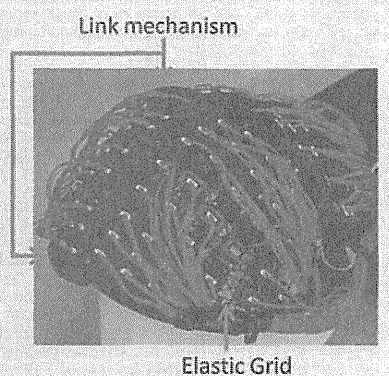

Fig. 3. Headset link mechanism and elastic grid

All the ADC modules, the mother-board and the battery are located in a wearable backpack. The headset weighted 745 g and the backpack weighted 1.80 kg. Data can be stored locally and visualized through an external display or PC.

B. Signal Processing System

EEG signals were recorded as a differential signal between a channel electrode and a reference electrode. Signal is amplified, filtered and sampled at 1 kHz at the 16 bit ADC modules. ADC modules simultaneously send the data to the motherboard CPU which stores the data on the memory. Using a different thread, the CPU sends the signal processing instructions and to the GPU.

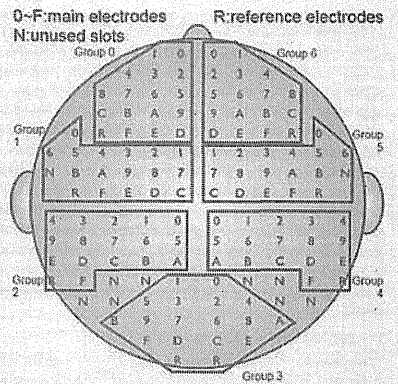

Fig. 4. Electrode placement method

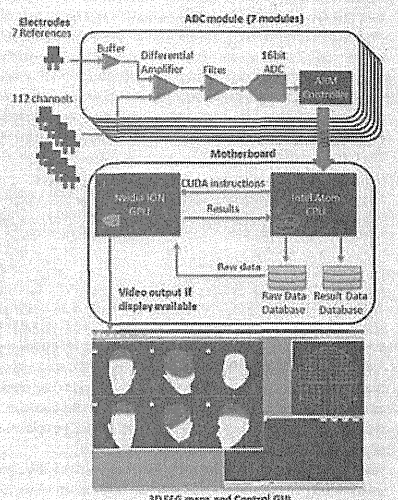

Fig. 5. Hardware elements and data flow diagram

In this preliminary study we demonstrate the capabilities of wearable GPU based processing for EEG monitoring by performing real time Fast Fourier Transforms (FFT) for all channels in real time on the GPU. Ideally, in our approach, we would perform a FFT based on the Cooley-Tukey algorithm for each channel using a separate GPU thread. However, due to the limitations on number of cores available in the used mobile GPU, we used the minimal recommend 32 CUDA threads, each thread performing the FFT from 4 channels. Because our system had only 112 channels, for code simplicity, we created an additional 16 dummy channels group with duplicated data from real channels to bring the total number of channels to 128. Channel data acquisition and result output is performed using the GPU direct memory access features. Each FFT was performed using the latest 1024 data samples for each channel, after each sampling cycle finished. FFT results are mapped on a human head 3D model for showing EEG signal strength at a chosen frequency at any point of the user's head. The 3D map can be visualized alongside the control graphical user interface for system by plugging in an external monitor or remotely accessing the systems.

C. EEG Monitoring Experiments

Two standard experiments monitoring EEG signals from different areas of the scalp were performed for device testing.

The first experiment consists in measuring brain activity changes above the frontal lobe due to visual stimuli. Previous studies have shown that when visual stimulus is weak, such as when the eyes are closed are the subject is in dark places, it's possible to record strong signals in the alpha band (8-13Hz) on the scalp area above the frontal lobe of the human brain[12][13]. In this experiment we perform EEG recordings by placing the participants on a dark room. A lamp was positioned in front of the participant and is used as an external source of light and visual stimuli. The lamp was turned on and off every 15 seconds during the total experiment time of 120 seconds.

The second experiment consists in measuring brain activity changes above the motor cortex that are due to hand and finger motions. When the participants' intention of movement is small, such as when the subject is at rest, it's possible to record strong signal on the 10 Hz u-rhythm frequency range, in the area above the motor cortex of the human brain. On the other hand, when the participant is moving one hand, u-rhythm gets weaker above the motor cortex opposite to the hand[14][15]. In this experiment we perform EEG recordings by placing the participants on a dark and silent room with the eyes closed. The subject stayed motion less for 30 seconds and then moved the right hand on a finger tapping movement, for another 30 seconds. This cycle was repeated 2 times for each experiment for a total experiment time of 120 seconds.

In order to evaluate the impact of the use of the GPU, both experiments were performed with and without using the CUDA features described in Section 2.2. The experiments were performed with 2 participants, each experiment was performed 3 times.

III. Results

A. Hybrid Electrodes

The noise spectrum in the 1-100 Hz band is shown in Fig. 6. The results show that noise is bellow 3 $\mu V/Hz^{1/2}$ for both resistive and capacitive modes. As EEG signals are in the order of 10-100 μV and commonly used signals oscillate in the 10-40 Hz band, the results show that our hybrid electrodes are reliable enough for EEG measurements.

B. EEG Monitoring Experiments

For the first experiment, the developed system was capable to record the data on both participants as expected from the results of previous researches. All electrodes showed strong signals when the light was turned off whereas a weak signal was recorded when the light was on. Fig.7 shows a sample spectrogram with the data collected by electrode 0 on group 0.

For the second experiment, the developed system was also capable to record the data on both participants and the results matching previous researches. For both participants, when the participant is performing the finger tapping motion, the electrodes C, D, E, F located on group 1 (Fig. 4) of the system, above the left motor cortex, recorded alpha band signals weaker than the when the participant was at rest. Fig. 8 shows the sample spectrogram for electrode C in group 1.

When experiments were executed with the CUDA features described in Section 2.2, the system was able to record data from all 112 channels at 1 kHz and perform FFTs for all channels after each sampling without delay or data loss. On the other hand, without using the CUDA features, thus allocating all the stress entirely on the CPU, the system took 400 ms to finish the FFTs for all channels and was unable to keep up with the 1 kHz sampling rate.

IV. Discussion

The experiments have shown that our electrodes were capable of recording both alpha waves and μ-rhythm without the need for skin preparation and that the results from our system are matched known brain activity phenomena. Our noise frequency analysis shows that our hybrid electrodes have a noise level below 3 $\mu V/Hz^{1/2}$, performing at similar levels to commercially available electrodes[8][16]. Both experiments suggest our system provides the high reliability required by professionals and end-users.

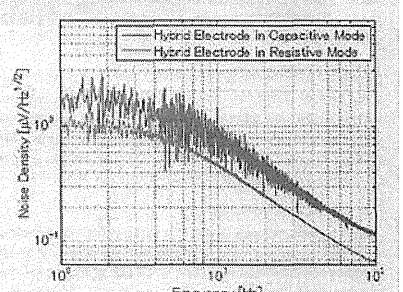

Fig. 6. Noise frequency spectrum

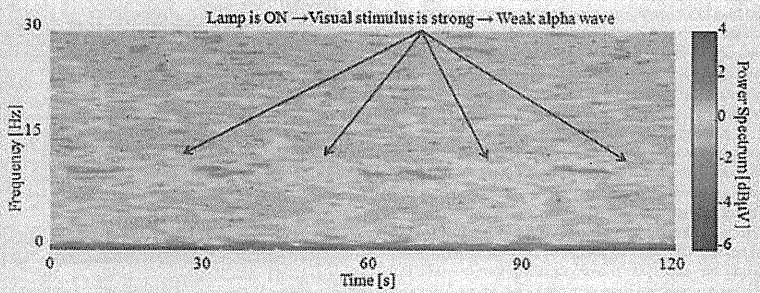

Fig. 7. EEG sample response to visual stimulus

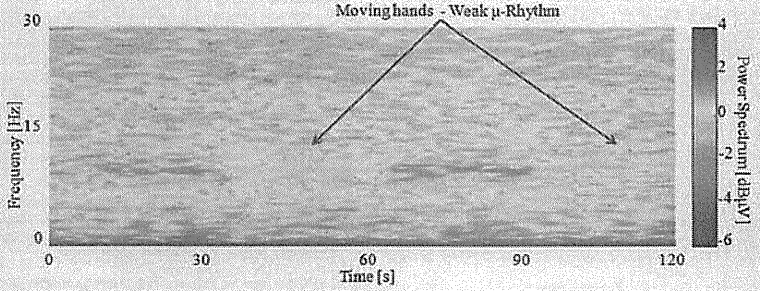

Fig. 8. EEG sample response to motor stimulus

With our hybrid electrodes removed the need of skin preparation, the wearability of the system was further increased by using a novel mechanism the allows the placement of over a hundred EEG electrodes over the users scalp simultaneously, thus reducing the time for wearing our 119 electrode system to up to 5 minutes, similar to the time required for 1-16 electrode systems[4]. Quick and easy electrode placement is fundamental for daily life usage, as it gives the user time to perform other activities while also it does not require specialized staff or training for correctly wearing the system. Furthermore, the lack of conductive gel and the problems associated with it such as signal degradation over time are completely avoided rendering battery capacity the only limiting factor for long continuous monitoring sessions. Using hybrid capacitive-resistive electrodes provided a high usability required by end users while also increasing the reliability of the system without reducing the spatial resolution of the sensor network.

The experiments have shown that our GPU based signal processing algorithm is powerful enough to perform FFTs for each channel after each sampling is finished, at 1 kHz sampling rate. While sampling at 1 kHz is a common practice, performing FFTs for each sampling at this rate is excessive considering the relatively low frequency EEG bioelectrical signals oscillate. However in this study, by showing that our system can perform heavy calculations at very fast rates, we show that our system perform in real time under heavy load by using algorithms optimized for parallel processing. On a realistic application scenario we can reduce the FFT execution and use the GPU processing power for other parallelizable tasks, such as neural networks[17]. Offloading signal processing to the GPU using CUDA not only allowed us to perform frequency analysis at real time but also freed the CPU for writing data to the hard-disk as well as displaying a fully interactive GUI with a 3D map of the EEG signals over the scalp. The high speed data processing allowed us to support a high spatial and temporal resolution which increase the reliability of the signal while leaving the CPU free for user interaction contributing in increasing the usability of the system. Furthermore, using a mobile GPU allowed us to have all these advantages in a wearable package, achieving a system with high portability and removed the need to have an external host PC, creating an all-in-one integrated system.

The data transfer between the electrodes and the GPU equipped mother-board was performed by seven 16-channel modules. This modular design allows users to add or remove at will. Taking advantage of this design professional users can perform experiments and development using high-density sensor networks, whereas when supplying the EEG monitoring system for the end user they can easily reduce hardware and optimize the system for the target application while still maintaining system consistence, thus reducing costs but offering a high application flexibility. In this study our system was a proof-of-concept prototype, thus also containing not optimized off-the-shelf parts, such as the motherboard containing the GPU. With the popularization of GPGPU capable System on Chip devices such as the Tegra 3 (Nvidia Corporation, USA) processor, further miniaturization and increase in power efficiency can be achieved in the near future.

EEG signals are used extensively on sleep disorder diagnosis and treatment, assistive device control and neurorehabilitation[1]-[3]. The effectiveness of some of these applications can be dependent on the frequency at which the patient uses EEG monitoring systems and is able to provide feedback to oneself as well as to the medical staff. While testing our new integrated system on a clinical environment is required, our tests with healthy participants suggest that the techniques in this study are a step forward in to increasing the impact of EEG technologies have in the medical field. Furthermore, the techniques introduced in this study can be extended towards other fields of wearable computing, robotics and medicine.

V. Conclusion

In this study we developed a novel integrated EEG monitoring system combining capacitive bioelectrical measurement and parallel computing technologies. A portable high-resolution EEG monitoring headgear composed of 112 sensing electrodes and 7 reference custom hybrid capacitive-resistive electrodes was developed. In order to record and analyze the massive amount of data from the headgear, a CUDA based wearable processing system was developed providing real-time signal analysis.

In future works we plan to optimize the hardware modular design of our system towards the creation of a EEG monitoring platform that can easily be customized by the users according to their needs as well as testing the device on clinical environments. We also extend the CUDA algorithms beyond real-time frequency analysis into a software platform for rehabilitation training feedback and assistive device interfacing as well as applying its principles to other wearable computing applications.

References

[1] M.L. Fantini, M. Michaud, N. Gosselin, G. Lavigne and J. Montplaisir: "Periodic leg movements in REM sleep behavior disorder and related autonomic and EEG activation", Neurology, Vol. 59, No. 12, 1889-1894 , 2002

[2] J.K. Chapin, K.A. Moxon, R.S. Markowitz, M.A.L. Nicolelis: "Real-time control of a robot arm using simultaneously recorded neurons in the motor cortex", Nature Neuroscience, Vol. 2, pp.664-670, 1999

[3] K.K. Ang, C. Guan, K.S.G. Chua, B.T. Ang, C. Kuah, C. Wang, K.S. Phua, Z.Y. Chin, H. Zhang: "Clinical study of neurorehabilitation in stroke using EEG-based motor imagery brain-computer interface with robotic feedback," 2010 Annual International Conference of the IEEE Engineering in Medicine and Biology Society, pp.5549-5552, 2010

[4] C.T. Lin, L.W. Ko, M.H. Chang, J.R. Duann, J.Y. Chen, T.P. Su, T.P. Jung, "Review of Wireless and Wearable Electroencephalogram Systems and Brain-Computer Interfaces – A Mini-Review." Gerontology, Vol. 56, pp. 112-119, 2010

[5] G. Schalk, D.J. McFarland, T. Hinterberger, N. Birbaumer, J.R. Wolpaw, "BCI2000: a general-purpose brain-computer interface (BCI) system," Biomedical Engineering, IEEE Transactions on , vol.51, no.6, pp.1034-1043, June 2004

[6] J.R. Wolpaw,N. Birbaumer,W.J. Heetderks,D.J. McFarland,P.H. Peckham,G. Schalk, E. Donchin, L.A. Quatrano, C.J. Robinson,T.M. Vaughan,"Brain-computer interface technology: a review of the first international meeting," IEEE Transactions on Rehabilitation Engineering,Vol.8, No.2, pp.164-173, 2000

[7] A. I. Ianov, H. Kawamoto, Y. Sankai, "Development of a Capacitive Coupling Electrode for Bioelectrical Signal Measurements and Assistive Device Use", Proceedings of the 2012 ICME International Conference on Complex Engineering, pp. 593-598, July, 2012

[8] A. I. Ianov, H. Kawamoto, Y. Sankai, "Development of Hybrid Resistive-Capacitive Electrodes for Electroencephalogram and Electrooculogram", IEEJ Transactions of Sensors and Micromachines, Vol. 133, No. 3, 2012(Accepted for publication, in press)

[9] J.A.Wilson, J.C. Williams, " Massively Parallel Signal Processing using the Graphics Processing Unit for Real-Time Brain–Computer Interface Feature Extraction", Front Neuroengineering, Vol. 2, Article 11, 2009

[10] A. Nukada, Y. Ogata, T. Endo, S. Matsuoka, "Bandwidth intensive 3-D FFT kernel for GPUs using CUDA," High Performance Computing, Networking, Storage and Analysis, 2008. SC 2008. International Conference for , pp.1-11, 15-21 Nov. 2008

[11] AIST,"RIO-DB: Available Database", http://riodb.ibase.aist.go.jp/dhbodydb/index.php.ja, March 6th, 2012 [September 14th, 2012]

[12] A. Craig, P. McIsaac, Y. Tran, L. Kirkup, A. Searle, "Alpha wave reactivity following eye closure: a potential method of remote hands free control for the disabled," Technology and Disability, Vol. 10, No. 3, pp. 187-194, January 1999

[13] A. Craig, Y. Tran, P. McIsaac, P. Moses, L. Kirkup, A. Searle. "The effectiveness of activating electrical devices using alpha wave synchronisation contingent with eye closure," Applied Ergonomics, Vol. 31, No. 4, pp. 377-382, August 2000

[14] A. R. Luft, S. McCombe-Waller, J. Whitall, L. W. Forrester, R. Macko, J. D. Sorkin, J. B. Schulz, A. P. Goldberg, D. F. Hanley, "Repetitive Bilateral Arm Training and Motor Cortex Activation in Chronic Stroke", JAMA., Vol. 292(15):1853-1861, 2004

[15] T. Balla, A. Schreibera, B. Feigeb, M. Wagnere, C. H. Luckinga and R. K. Feig, "The Role of Higher-Order Motor Areas in Voluntary Movement as Revealed by High-Resolution EEG and fMRI," NeuroImage, Vol. 10(6), pp. 682-694, 1999

[16] Y.M. Chi, T.P. Jung, G. Cauwenberghs: "Dry-Contact and Noncontact Biopotential Electrodes: Methodological Review", IEEE Reviews in Biomedical Engineering, Vol.3, pp.106-119 , 2010

[17] H. Jang, A. Park, K. Jung, "Neural Network Implementation Using CUDA and OpenMP," Computing: Techniques and Applications, 2008. DICTA '08.Digital Image, pp.155-161, 1-3 Dec. 2008

2012 IEEE/RSJ International Conference on
Intelligent Robots and Systems
October 7-12, 2012. Vilamoura, Algarve, Portugal

Pilot study of floor-reactive-force generator mounted on MRI compatible lower-extremity motion simulator

IKEDA Takahiro, MATSUSHITA Akira, SAOTOME Kosaku, HASEGAWA Yasuhisa and SANKAI Yoshiyuki

Abstract— **This paper describes a novel motion simulator for the lower extremities of human in a magnetic resonance imaging (MRI) environment. This motion simulator provides a wearer with physical supports to move their lower extremities or physical constrains as well as floor reactive force on bottoms of their feet during gait-like motion in an MRI room so that brain activities could be simultaneously measured. An MRI is one of the most powerful tools to measure activities in any part of brain but a device attached on a subject is limited because the material used for the device should be nonmagnetic. This paper shows the compatibility of the motion simulator that consists of Mckibben-type pneumatic artificial muscles and nonmagnetic materials. Also this paper shows the performance of the floor-reactive-force generator mounted on the soles of the motion simulator.**

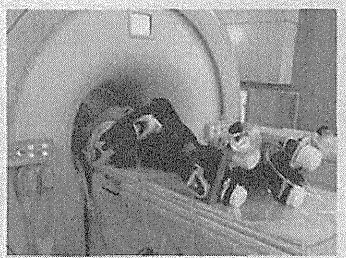

Fig. 1. Lower-extremity motion simulator (LoMS) in MRI.

I. INTRODUCTION

This paper describes the new wearable lower-extremity motion simulator (LoMS; Fig. 1) that can be used in high magnetic field. LoMS enables a magnetic resonance imaging (MRI) system to measure brain activities of a human subject while their lower extremities are engaged in active and passive motion. Functional MRI (fMRI) is an optimal tool for measuring brain activation related to lower-extremities motion, because related activation typically occurs in deep brain regions. An fMRI is a powerful tool for measuring human brain activity because the depth of measurement with fMRI is greater than that of other techniques such as an electroencephalograph (EEG) and a near-infrared spectroscopy (NIRS). An EEG provides a measure of the electrical potential on the surface of the scalp, while a NIRS measures changes in hemoglobin concentration in the superficial layer of the brain. Both EEG and NIRS observe activities in a surface layer of a brain. On the other hand, an MRI can measure activation at the whole brain level. Thus, an MRI is employed for measurement of brain activities related to a lower-extremity motion in our study.

Revealing relationships between the human brain and lower extremities during active and passive motions is helpful for the development of effective rehabilitation techniques. Rehabilitation is essential for patients whose physical functions have been damaged by stroke or other brain injury, to aid them in performing various activities of daily life. Importantly, neurorehabilitation techniques based on developments in neuroscience can provides new methods by which to assess the benefits of rehabilitation using neuroscientific knowledge. To develop new neurorehabilitations techniques, it is important to determine how the brain is activated during motion, sensation and conception. LoMS can generate subject motion, like that generated by robots used in robot therapy as tools for rehabilitation. In addition, LoMS can be used when the brain activity of a wearer is measured by MRI during lower-extremity motion. Therefore, LoMS can reveal effective motions as robot therapy with a point of view of neurorehabilitation.

A number of previous studies have focused on human brain activity related to lower-extremity motion. For example, several studies have examined brain activation induced by ankle joint movement using fMRI (Sahyoun et al. 2004 [1], O. Ciccarelli et al. 2005 [2], Btuce H. Dobkin et al. 2004 [3]). These studies typically employ a wooden apparatus to extend or flex an ankle joint, reporting a relationship between brain activation and preparation for active motion or anticipation for passive motion. It was revealed that the brain was strongly activated during preparation or anticipation. Thijs et al. reported that bracing a knee joint influences a brain activity (Thijs 2010 [4]), finding that cortical activation was increased when a knee joint was braced more strongly during its movement. However, these previous studies have focused on a single joint, and few studies have examined the brain activity associated with a simultaneous movement in multiple joints. In addition, several studies have examined brain activation during pedaling locomotion (Kautz et al. 1998 [5], Mehta et al. 2009 [6]). In these studies, the motion enabled by experimental apparatus is limited to specific type of movement (pedaling), and cannot provide information about multiple types of motion in the human lower extremities. In these previous studies, the devices involve only one degree of freedom for the execution of lower-extremity motion.

Recent research within our group has focused on brain activities and the transitions of the brain activities observed during a gait-like motion and other various movements of lower extremities. The purpose of the current paper is therefore to develop a motion simulator for lower extremities called LoMS that enables various active and passive movements of the user's lower extremities in an MRI environment. This paper introduces the LoMS system, and reports experimental confirmation that LoMS does not have adverse effects on the functionality of MRI and testing the use of joint angle measurement in the MRI acquiring environment. In addition, floor reactive force is essential sensory feedback for human when they moves their lower extremities. Floor reactive force enables human to cognize contacts between their foot and a floor and their center of gravity. Therefore, Floor reactive force has to be given to a subject while simulating lower-extremity motion. LoMS is implemented floor-reactive-force generating parts and the the performance of this generating parts are reported in this paper.

IKEDA T. is with Department of Intelligent Interaction Technologies, Graduate School of System and Information Engineering, University of Tsukuba, Tsukuba, Ibaraki, Japan. ikeda.kikou@gmail.com

MATSUSHITA A. is with Center for Cybernics Research, University of Tsukuba, Tsukuba, Ibaraki, Japan. akira@ccr.tsukuba.ac.jp

SAOTOME K. is with Center for Cybernics Research, University of Tsukuba, Tsukuba, Ibaraki, Japan. saotome@ccr.tsukuba.ac.jp

HASEGAWA Y. is with Department of Intelligent Interaction Technologies, Graduate school of System and Information Engineering, University of Tsukuba, Tsukuba, Ibaraki, Japan. hase@esys.tsukuba.ac.jp

SANKAI Y. is with Department of Intelligent Interaction Technologies, Graduate school of System and Information Engineering, University of Tsukuba, Tsukuba, Ibaraki, Japan. sankai@kz.tsukuba.ac.jp

978-1-4673-1735-1/12/$31.00 ©2012 IEEE

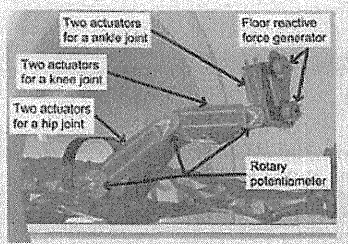

Fig. 2. Drive mechanism: Each joint has two Mckibben-type pneumatic artificial muscles for extension and flexion, using a rotary potentiometer. A couple of the pneumatic muscles is mounted on a thigh to drive a hip joint. Similarly, a couple is mounted on a shank for knee joint drive and one is mounted on a foot for ankle joint drive. Each sole has two piston to generate floor reactive force against foot.

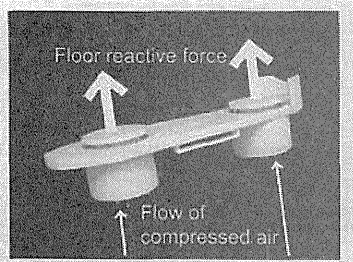

Fig. 4. Floor-reactive-force generator(FRF generator): LoMS has two pistons at each sole to simulate floor reactive force. Compressed air is provided into the pistons from the bottom. One of the pistons is on the thenar region of the sole and another is on the heel region. The FRF generator gives a subject a sense of the position of center of gravity.

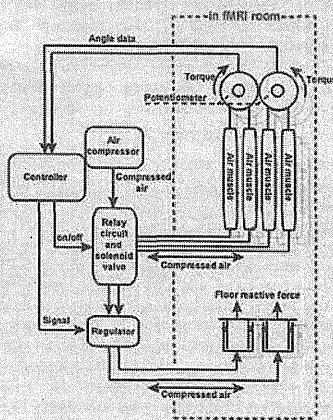

Fig. 3. System architecture: Magnetic materials(an air compressor, solenoid valves, electropneumatic regulators and a controller)are located outside the MRI room. Only nonmagnetic materials are located within the MRI room, for safety.

II. LOWER-EXTREMITY MOTION SIMULATOR (LOMS)

The system architecture of LoMS is described in detail in our previous paper[7]. Therefore, only the essentials of the system architecture is explained in this section.

Since an MRI uses a high magnetic field, LoMS is constructed from nonmagnetic materials to meet following criteria:

- The equipment functions properly in the high magnetic field of the fMRI environment.
- The equipment does not adversely affect the image quality of fMRI acquisition.

The joint components are constructed from acrylonitrile butadiene styrene (ABS). Other parts of frame are constructed from nonmagnetic stainless steel (SUS304), while the cover is constructed from acrylic. The system also requires a nonmagnetic actuator. As such, Mckibben-type pneumatic artificial muscles (Airmuscle:KANDA TSUSHIN KOGYO CO., LTD., Tokyo, Japan) are employed for the actuators of LoMS' joints. A joint angle is measured by a rotary potentiometer(SV01:Murata Manufacturing Co., Ltd.,

Fig. 5. Experiment using the test model of LoMS in the MRI environment: The LoMS system used for testing consisted of all parts except the pneumatic actuators.

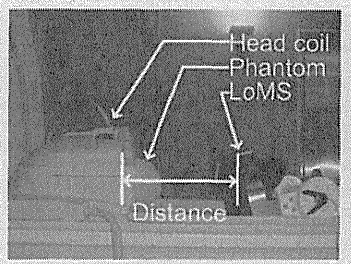

Fig. 6. Magnetic susceptibility artifact assessment: The assessment was conducted with a phantom subject.

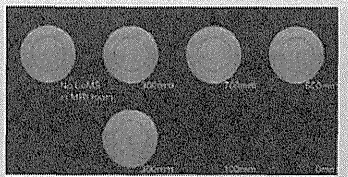

Fig. 7. T_2 images of a phantom subject when the distance between the LoMS system and the head coil was changed: When the distance was shorter, the signal intensity of phantom is lower and the image appears dark. If the signal intensity is high, the image is bright.

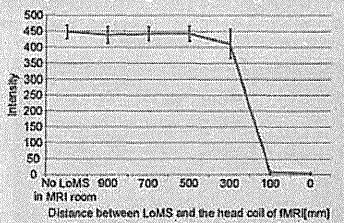

Fig. 8. The signal intensity of fMRI scan with a phantom subject related to the distance between the LoMS system and the head coil: The signal intensity is calculated by averaging each signal intensity of a voxel in the red circle in Fig. 7. LoMS is just set, not working.

Kyoto, Japan) that is made from conductive plastic and nonconductive plastic. LoMS has three degrees of freedom per leg, at the hip joint, knee joint and ankle joint(Fig. 2). Two Mckibben-type pneumatic artificial muscles actuate each joint for extension and flexion. Each Mckibben-type pneumatic muscle has three states, inflowing, outflowing and holding compressed air, with two two-stage three-port type solenoid valves. A controller (SH4:General Robotix, Ibaraki, Japan), an air compressor and the solenoid valves are located outside of the MRI room(Fig. 3). LoMS has foot stimulating parts at its two soles to simulate floor reactive force (Floor-reactive-force generator: FRF generator(Fig. 4)). FRF generator is also constructed from nonmagnetic materials: ABS, acrylic, SUS304 and rubber. FRF generator contains two piston parts on each sole to press a subject's sole like floor reactive force. The pistons are driven by compressed air flowing in them from the bottoms. These two pistons are also designed to make subject feel translation of their center of gravity in the longitudinal direction.

III. Compatibility Assessment

Three assessments of MRI compatibility were executed by LoMS, not including the artificial muscles and FRF generators, and an MRI scanner (Achieva 3.0T TX, Philips, Eindhoven, Nederland) with 32-channel head coil(Fig. 5).

A. Magnetic susceptibility artifact assessment

First, we sought to test whether LoMS exerted an adverse effect on the magnetic field quality of an MRI scan (Fig. 6). The subject was a head phantom filled with cupric sulfate solution. The effect of LoMS was evaluated by the signal intensity and its dispersion of the phantom image. Figure 7 shows the phantom images and regions of interest (ROI) that were measured. Figure 8 shows relationships between the signal intensity in the ROI and the distance between the head coil and LoMS. There was no available image when the distance was less than 300[mm] and the signal intensity and its dispersion were almost the same in the images when the distance was more than 500[mm]. When a subject wears the LoMS system, the distance of LoMS from the head coil ranges from almost 500 to 700[mm]. Thus, the influence of LoMS does not appear to substantially disrupt the evaluation of head images of a subject wearing the LoMS system.

B. Functional imaging assessment

Secondly, brain activities were then imaged during lower-extremity motion in two cases, as follows:

Case 1. When the subject did not wear LoMS.
Case 2. When the subject wore LoMS.

The task consisted of four repetitions of thirty-second rest and thirty-six-second reciprocal motion. The reciprocal

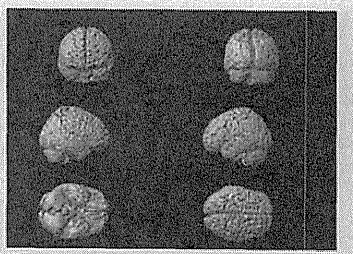

Fig. 9. Functional images when the subject moved the lower extremities voluntarily while not wearing LoMS: The strongest activation was observed in the primary motor cortex and the supplementary motor cortex.

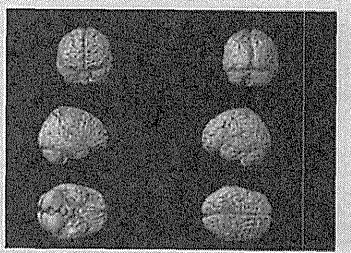

Fig. 10. Functional images when the subject moved one's lower extremities voluntarily wearing LoMS: The activation was observed in the primary motor cortex and the supplementary motor cortex, but with some difference patterns of activity in other areas. This is because the magnetic field of fMRI is influenced by LoMS more than a little.

motion was repetition of flexion and extension of lower extremities. The functional image in case 1 is shown in Fig. 9 and one in case 2 is shown in Fig. 10. In Fig. 9, the activations were observed in the primary motor area, supplementary motor area and the cerebellum dominantly. These areas are related to lower-extremity motion. In Fig. 10, the activations were observed in the same area as case 1, but some activations were also observed at other areas. Therefore, the measured activations may be affected by the presence of LoMS or a subject wearing LoMS. However, an assessment of magnetic susceptibility artifacts indicated that brain activity could be measured in case 2, as in case 1. Careful examination of of brain activity revealed that the areas related to lower-extremity motion were activated to a much greater extent than other areas. These findings suggest that an increased activation threshold may be appropriate, so that the activation changes of interest can still be observed in the area, as in case 1, Fig. 11. Overall, fMRI imaging appeared to function adequately with a subject wearing LoMS and moving their body.

C. Motion capturing assessment

A third test was conducted to confirm that the motions of subject's lower extremities could be measured with accuracy

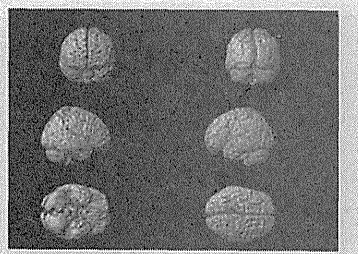

Fig. 11. Functional images reproduced from Fig. 10 with a harder threshold: The activations of interest were observed in the areas related to lower-extremity motion, and activations in other areas were reduced.

in an fMRI environment. In this test, LoMS was not worn and the hip joints were moved by the experimenters. The hip joint can flex to a maximum of 110[deg] and extend to a maximum of 15[deg]. The experimenters moved the joint peak to peak in the range of the joint. The angles of hip joints were measured by each potentiometer with low-pass filters(the cut-off frequency is 10.6[Hz]) in two cases as follows:

Case 1. When LoMS operates in a normal environment.
Case 2. When LoMS was in the MRI room during fMRI measurement. This means that LoMS is under a static high magnetic field and there is the electromagnetic wave(RF pulse) generated by the body coil.

The measured trajectory of the hip joints in case 1 is shown in Fig. 12(a). The peak-to-peak angle of the right hip joint is 126.5[deg] and that of the left hip joint is 128.1[deg] as measuring results. The captured trajectory of the hip joints in case 2 is shown in Fig. 12(b). The peak-to-peak angle of the right hip joint is 126.0[deg] and that of the left hip joint is 127.4[deg]. In case 2, there was no noise attributed to the RF pulse generated by the body coil. Table I shows peak-to-peak angles and error rates. The results indicate that LoMS can capture lower-extremity motion in an fMRI environment because the error rates are small enough to measure the joint angles.

IV. Performance of Floor-Reactive-Force Generator

FRF generator was evaluated in generating forces related to compressed air and center-of-gravity (COG) position control. Figure 13 shows the relationship between the generating force and provided air pressure. The generating force is proportional to air pressure. The maximum generating force is about 330[N] when 0.5[MPa] compressed air is provided. Figure 14 shows the position of COG controlled by the floor-reactive-force generator with blue line and the force generated by the floor-reactive-force generator with red line. The position of COG was measured from the heel. The position of COG was able to be controlled from the heel

TABLE I

CAPTURED PEAK-TO-PEAK ANGLES AND ERROR RATES

Measuring case	Captured peak-to-peak angle[deg]		Error rate against case 1[%]	
	Right hip joint	Left hip joint	Right hip joint	left hip joint
Case 1	126.50	128.13	-	-
Case 2	126.02	127.36	0.37820	0.59373

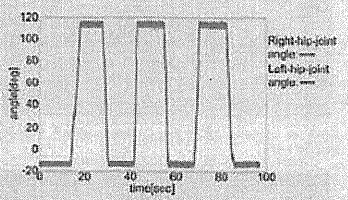

(a) The trajectories when LoMS was outside the MRI environment: The rotation angle of the joint is limited from -15 to 110[deg].

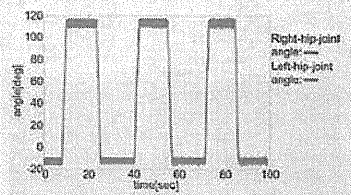

(b) The trajectories while fMRI executed scanning: The rotation angle of the joint is limited from -15 to 110[deg].

Fig. 12. The trajectories of the hip joint angles when LoMS was moved by the experimenter.

to the toe and from the foe to the heel in the constant speed. As a result, the position of COG can be controlled arbitrarily by floor-reactive-force generator.

V. EXPERIMENT ON BRAIN ACTIVITY WITH FLOOR REACTIVE FORCE

A. Experimental protocol

A experiment on brain activity with floor reactive force was executed by LoMS with FRF generators and MRI scanner (Achieva 3.0T TX, Philips, Eindhoven, Nederland) with 32-channel head coil. 10 healthy-twenties men were volunteered as subjects. A subject moved their lower extremities voluntarily wearing LoMS. The scanning session consisted of eight repetitions of thirty-second rest and thirty-six-second task. The task was repetition of flexion and extension of lower extremities. The tasks were executed in following state:

Case 1. With floor reactive force.

Case 2. Without floor reactive force.

The floor reactive force was provided by floor-reactive-force generators in each task in random order. Totally, floor reactive force was provided in four tasks and was not provided in four tasks.

B. Experimental results

Figure 15(a) shows the brain activity in case 1. Figure 15(b)shows the brain activity in case 2. In each case, the motor cortex and the cerebellum are activated especially. At the motor cortex, the activation with floor reactive force is different from the activation without floor reactive force and, any region of the brain proper to floor reactive force is observed. Subject's impressions about floor reactive force were separated into positive impressions and negative impressions. Floor reactive force helped some subjects to recognize that their lower extremities were extended. On the other hand,

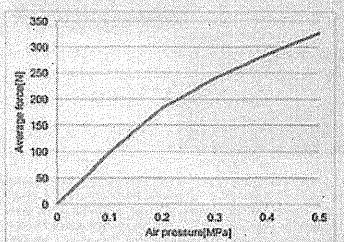

Fig. 13. Relationship between average force generated by FRF generator and air pressure: The generated force is proportional to the supply pressure.

the timing of floor-reactive-force stimulation was discrepant to the intuitions of some subjects.

VI. CONCLUSION

This study assessed the compatibility of LoMS with an MRI, from three functional perspectives; magnetic susceptibility artifacts, functional imaging and capturing human motion. Also, this study evaluated the performance of FRF generator of LoMS. In addition, a pilot experiment on brain activity with floor reactive force was executed. Our LoMS system was designed to simulate passive and active gait-like motion in MRI acquisition. Three experimental tests confirmed that the quality of MRI was not strongly affected by the presence and motion of LoMS, and that LoMS was able to capture human motion using rotary potentiometers through the low-pass filters without any adverse effects from the RF pulse of MRI. FRF generator was also evaluated for the generating force and the COG position control. FRF

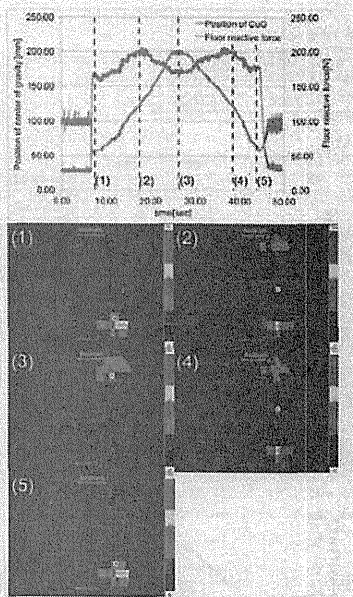

Fig. 14. Position of center of gravity and floor reactive force generated by floor-reactive-force generator: In the graph, the blue line is the trajectory of position of center of gravity. Position of center of gravity is measured from the heel(0[mm]) to the toe(250[mm]). The red line is the floor reactive force against the whole right sole. Five figures below the graph show the center of gravity with white circle and floor reactive force in color as pressure at each area of LoMS ' sole.

generator can provide a wearer the position of COG. In the experiment on brain activity with floor reactive force, the activation with floor reactive force at the motor cortex was different from the activation without floor reactive force and, any region of the brain proper to floor reactive force was observed. Some subjects had negative impressions such as the discrepancy between the timing of floor-reactive-force stimulation and the intuitions of subjects. Thus, improving the timing is a possible future work.

ACKNOWLEDGMENTS

This study was supported by the "Center for Cybernics Research (CCR) - World Leading Human-Assistive Technology Supporting a Long-Lived and Healthy Society'" granted through the "Funding Program for World-Leading Innovative R&D on Science and Technology (FIRST Program)," initiated by the Council for Science and Technology Policy (CSTP).

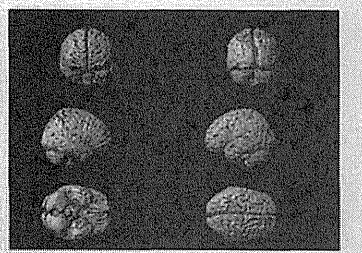

(a) Brain activation during lower-extremity motion with floor reactive force.

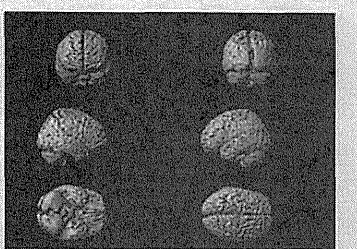

(b) Brain activation during lower-extremity motion without floor reactive force.

Fig. 15. Brain activity with or without floor reactive force: When 10 subjects moved their lower extremities with floor reactive force and without floor reactive force, the motor cortex and the cerebellum were activated. There were no significant difference between the regions of two cases.

REFERENCES

[1] C. Sahyoun, A. Floyer-Lea, H. Johansen-Berg, P.M. Matthews, "Towards an understanding of gait control: brain activation during the anticipation, preparation and execution of foot movements," *NeuroImage 21* , 2004, pp.568-575

[2] O. Ciccarelli, A. T. Toosy, J. F. Marsden, C. M. Wheeler-Kingshott, C. Sahyoun, P.M. Matthews, D. H. Miller, A. J. Thompson, "Identifying brain regions for integrative sensorimotor processing with ankle movements," *Exp Brain Res*, 166, 2005, pp. 31-42

[3] Bruce H. Dobkin, Ann Firestine, Michele West, Kaveh Saremi, Roger Woods, "Ankle dorsiflexion as an fMRI paradigm to assy motor control for walking during rehabilitation," *NeuroImage*, 23, 2004, pp. 370-381

[4] Youri Thijs, Guy Vingerhoets, Els Pattyn, Lies Rombaut, Erik Witvrouw, "Does bracing influence brain activity during knee movement: an fMRI study," *Knee Sports Traumatol Arthrosc* , 2010, 18, pp.1145-1149

[5] S.A. Kautz, D.A. Brown, "Relationships between timing of muscle excitation and impaired motor performance during cyclical lower extremity movement in post-stroke hemiplegia," *Brain*, 1998, 121, pp.515-526

[6] Jay P. Mehta, Matthew D. Verber, Jon A. Wieser, Brain D. Schmit, Sheila M.Schindler-Ivens, "A novel technique for examining human brain activity associated with pedaling using fMRI," *Journal of Neuroscience Methods*, 179, 2009, pp.230-239.

[7] IKEDA Takahiro, MATSUSHITA Akira, SAOTOME Kosaku, HASEGAWA Yasuhisa, SANKAI Yoshiyuki, "Compatibility test on lower-extremity motion simulator to fMRI," *Proceedings of the 2011 IEEE International Conference on Robotics and Biomimetics*, 2011, pp. 56-61.

学術・技術論文

アクティブエアマットによる支援機器の親和性の改善

長谷川 泰 久*1 田 山 宗 徳*2 齊 藤 壮 文*2
長谷川 誉 晃*2 山 海 嘉 之*1

Affinity Improvement of Support System by Use of Active Air Mattress

Yasuhisa Hasegawa*1, Munenori Tayama*2, Takefumi Saito*2,
Takaaki Hasegawa*2 *and* Yoshiyuki Sankai*1

This paper proposes an active air mattress to improve affinity of an upper limb support system. The affinity is developed by several items. An easiness of an attaching and releasing process of the support system contributes to a short-term affinity. Comfortableness and sense of belonging during wear belongs to a long-term affinity. Both are very important in addition to support functions of the system. The active air mattress installed in a forearm part of the support system actively holds a human forearm quickly and firmly, and then changes the contacting areas with a human skin in order to maintain adequate blood circulation around the contacting area. Exhaust air from air chambers is reused to ventilate around a forearm skin. It is evaluated through some experiments from viewpoint of pressure distribution, blood flow, wearing time, releasing time, body-holding rigidity, temperature and humidity of a human skin.

Key Words: Affinity, Air Mattress, Easiness, Comfort, Support System

1. はじめに

高齢者は筋骨格系の衰えにより把持力などの筋力が低下し[1]，日常生活で不便さが生じる場面が多くなる．そのため，人による介護だけでなく，機器による介護が重要となる．そこで，高齢者などを対象にその動作を支援するシステムが研究されている[2][3]．このような支援機器の持つ支援機能は，システムの有用性で大変重要な点であるが，システムを身体に装着する場合には，身体へのシステムの親和性もシステムを評価する上で重要な項目となる．この親和性とは，着脱の容易さや身体へのフィット感・一体感に代表される短期的な側面と，血行や湿度などの長期的な側面に分類できる．例えばより人が装着しやすく，また装着者の動作を妨げないようにする機械的な構造の提案[4]が行われているが，筆者の知る限りでは，短期・長期親和性を両立する機構の提案はこれまでに行われていない．支援を必要とする人々は一般的に身体の運動機能が低下しているために，システムの装着作業自身が大きな負担となる場合が少なくない．また，運動麻痺部位にシステムを装着した場合には，身体の重量を支える部分に自重により圧力が長期にわたり同一部位に集中してしまい，その部位では血流が阻害され，最悪の場合，褥瘡が生じてしまうことがある．これは，人間の毛細血管内圧は32 [mmHg] 程度と動脈と比べて低く，それ以上の圧力が加わると毛細血管が閉塞状態になり皮膚組織に血が通わなくなってしまうからである[5]．それに加え，システムを長時間装着することにより温度・湿度が上昇し不快感の増大が起きたり，細菌の増殖が生じたりする危険性がある．よって，これらの問題点を解決できる親和性の高い運動支援システムが望ましい．一方，健常者が作業軽減のために運動支援システムを装着する場合にも，何度も着脱を繰り返すことなく長時間快適に装着できることが望ましい．そこで，本論文では，支援システムを容易に短時間で装着でき，長時間装着しても不快とならない短期・長期親和性を両立する機構の実現のため，アクティブエアマットを提案する．また，本アクティブエアマットを外骨格型前腕支援システムに搭載し，その親和性の評価をし，その有効性の検証を行う．

原稿受付 2011年12月9日
*1筑波大学システム情報系
*2筑波大学大学院システム情報工学研究科
*1University of Tsukuba
*2Department of Intelligent Interaction Technologies Graduate School of Systems and Information Engineering, University of Tsukuba
■ 本論文は有用性で評価されました．

2. システム全体概要

2.1 前腕支援システム

本論文で提案するアクティブエアマットの性能を評価するために，Fig. 1に示す外骨格型前腕支援システム[6]を用いる．本支援システムはFig. 2に示すように手装着部，前腕装着部，上腕装着部の三つの拘束部位から構成され，それらの部位の間では手関節および肘関節の運動を支援するものとなっている．手装着部は母指，示指，その他3指（中指，薬指，小指）が独立に屈曲動作が支援され，この3指は同時に屈曲を行う．示指とその他3指（中指，薬指，小指）の屈曲動作は，各三つのモータを用いて，ワイヤを介して駆動される．また，母指は屈曲動作だけでなく対立動作もワイヤおよびリンク機構にてDCモータにより支援する．前腕装着部には手首動作と肘屈曲を支援するモータを内蔵し，手首動作の回内，回外，屈曲，背屈および，肘屈曲動作を支援する．モータドライバと電磁弁もこの前腕装着部に内蔵されている．提案するアクティブエアマットもこの前腕装着部の内側面に搭載され，装着者の前腕を適切に保持する．上腕装着部には二つのマイコンが搭載されており，本システムの14個のDCモータ，13 [ch] のポテンショメータ，6 [ch] の生体電位信号および3個の電磁弁を制御している．人間の手は細かな作業から力を必要とする重作業まで非常に幅広い力の制御範囲を持っている．しかし，力支援は，大きな力が必要な作業時に行うことが合理的であり，細かな作業時には，人の作業を支援システムが妨げないようにすることが重要である．これは手首と肘の動作でも同様である．したがって，生体電位に基づく人の動作への追従制御と人の各関節のトルク支援制御の二つの制御モードを切り替える生体電位に基づくスイッチング制御を行う．トルク支援制御モードでは，対応する筋肉の生体電位の積分値が閾値（C_2）を超えた場合のみ，積分値に比例した関節トルクを支援する．この生体電位（Integral BioElectric Potential：IBEP）は次の式で求められる．

$$IBEP(t) = \int_{t-T}^{t} bep(i)di, \qquad (1)$$

t は時間，T は積分時間，$bep(i)$ は時間 i における生体電位である．対応する筋肉の生体電位の積分値が閾値（C_1）を下回った場合は追従制御モードとなり，駆動ワイヤの張力がほぼゼロになるようにポテンショメータを用いてDCモータを制御することで，外骨格の各関節を自由に動かすことができる．生体電位がこれらの閾値 C_1 と C_2 の中間の値の場合には，直前のモードを継続する．その制御モードのブロック図をFig. 3に示す．

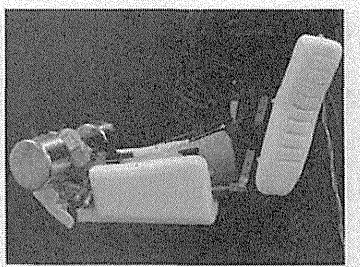

Fig. 1 Forearm support system

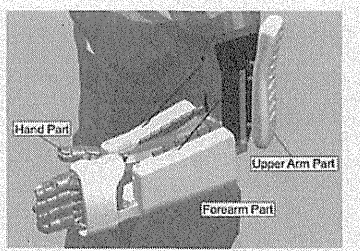

Fig. 2 Components of forearm support system

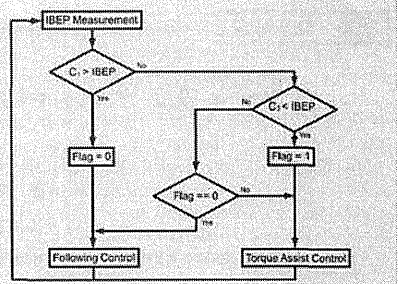

Fig. 3 Bioelectric potential-based switching control

2.2 アクティブエアマット

褥瘡とは皮膚が壊死する病態であり，皮膚潰瘍の一つである．主な原因として，持続的な圧迫による血行不良や湿潤によるものから，加齢や低栄養などによるものがある．特に骨が突出しており脂肪や筋肉の薄い部位において，毛細血管圧である32 [mmHg] 以上の体圧が持続的に加わると発症しやすいといわれている[5]．また，一度褥瘡が発症すると完治には非常に時間がかかるため，褥瘡予防の研究が行われているが[7][8]，これらはエアマットやエアクッションなどの寝姿勢や座位姿勢時におけるものであり，装着型の支援システムには適用されていない．また，仙骨部や大転子部，坐骨部などには体重が集中しやすく，発症しやすいとされているが，前腕支援システムにおいても，長時間装着し静止した状態でいることを考えれば，肘などにも十分発症の危険性がある．そのため，支援システムにも褥瘡予防を考慮する必要があるといえる．そこで，本研究では外骨格型前腕支援システムにアクティブエアマットを搭載することにより，その問題点の改善を行う．

アクティブエアマットとは，独立した複数のエアー室が膨張と収縮を繰り返すことによって能動的に体圧の分散および血行促進，皮膚表面の強制換気を行うエアマットである．Fig. 4に示すように，本支援システムではこのアクティブエアマットを装着者の前腕部と接触する前腕装着部に搭載する．本アクティブエアマットは，Fig. 5 (a) に示すように独立した3系統（A, B, C）の空気室を2セット有し，システム外部のコンプレッサからの給気を電磁弁で制御することによって膨張と収縮を行う．